manuscript, Noriko Hitosugi for technical assistance, and Judith Nishino for helpful discussions during the preparation of this manuscript.

References

Al-Ani B and Hollenberg MD (2003) Selective tryptic cleavage at the tethered ligand site of the amino terminal domain of proteinase-activated receptor-2 in intact cells. *J Pharmacol Exp Ther* **304**:1120–1128.

Al-Ani B, Saifeddine M, Kawabata A, and Hollenberg MD (1999) Proteinase activated receptor 2: Role of extracellular loop 2 for ligand-mediated activation. *Br J Pharmacol* **128**:1105–1113.

Bacman S, Berra A, Sterin-Borda L, and Borda E (2001) Muscarinic acetylcholine receptor antibodies as a new marker of dry eye Sjogren syndrome. *Investig Ophthalmol Vis Sci* **42**:321–327.

Belting M, Dorrell MI, Sandgren S, Aguilar E, Ahamed J, Dorfleutner A, Carmeliet P, Mueller BM, Friedlander M, and Ruf W (2004) Regulation of angiogenesis by tissue factor cytoplasmic domain signaling. *Nat Med* **10**:502–509.

Bivona PL (1998) Xerostomia. A common problem among the elderly. *NY State Dent J* **64**:46–52.

Camerer E, Rottingen JA, Iversen JG, and Prydz H (1996) Coagulation factors VII and X induce Ca^{2+} oscillations in Madin-Darby canine kidney cells only when proteolytically active. *J Biol Chem* **271**:29034–29042.

Corvera CU, Dery O, McConalogue K, Bohm SK, Khitin LM, Caughey GH, Payan DG, and Bunnett NW (1997) Mast cell tryptase regulates rat colonic myocytes through proteinase-activated receptor 2. *J Clin Investig* **100**:1383–1393.

Dawson LJ, Stanbury J, Venn N, Hasdimir B, Rogers SN, and Smith PM (2006) Antimuscarinic antibodies in primary Sjogren's syndrome reversibly inhibit the mechanism of fluid secretion by human submandibular salivary acinar cells. *Arthritis Rheum* **54**:1165–1173.

Dery O, Corvera CU, Steinhoff M, and Bunnett NW (1998) Proteinase-activated receptors: novel mechanisms of signaling by serine proteases. *Am J Physiol* **274**: C1429–C1452.

Ekstrom J (1987) Neuropeptides and secretion. *J Dent Res* **66**:524–530.

Ferrell WR, Lockhart JC, Kelso EB, Dunning L, Plevin R, Meek SE, Smith AJ, Hunter GD, McLean JS, McGarry F, et al. (2003) Essential role for proteinase-activated receptor-2 in arthritis. *J Clin Investig* **111**:35–41.

Futatsugi A, Nakamura T, Yamada MK, Ebisui E, Nakamura K, Uchida K, Kitaguchi T, Takahashi-Iwanaga H, Noda T, Aruga J, et al. (2005) IP_3 receptor types 2 and 3 mediate exocrine secretion underlying energy metabolism. *Science (Wash DC)* **309**:2232–2234.

Grynkiewicz G, Poenie M, and Tsien RY (1985) A new generation of Ca^{2+} indicators with greatly improved fluorescence properties. *J Biol Chem* **260**:3440–3450.

Hollenberg MD, Laniyonu AA, Saifeddine M, and Moore GJ (1993) Role of the amino- and carboxyl-terminal domains of thrombin receptor-derived polypeptides in biological activity in vascular endothelium and gastric smooth muscle: evidence for receptor subtypes. *Mol Pharmacol* **43**:921–930.

Kawabata A, Kanke T, Yonezawa D, Ishiki T, Saka M, Kabeya M, Sekiguchi F, Kubo S, Kuroda R, Iwaki M, et al. (2004a) Potent and metabolically stable agonists for protease-activated receptor-2: evaluation of activity in multiple assay systems in vitro and in vivo. *J Pharmacol Exp Ther* **309**:1098–1107.

Kawabata A, Kawao N, Itoh H, Shimada C, Takebe K, Kuroda R, Masuko T, Kataoka K, and Ogawa S (2002a) Role of *N*-methyl-D-aspartate receptors and the nitric oxide pathway in nociception/hyperalgesia elicited by protease-activated receptor-2 activation in mice and rats. *Neurosci Lett* **329**:349–353.

Kawabata A, Kinoshita M, Nishikawa H, Kuroda R, Nishida M, Araki H, Arizono N, Oda Y, and Kakehi K (2001) The protease-activated receptor-2 agonist induces gastric mucus secretion and mucosal cytoprotection. *J Clin Investig* **107**:1443–1450.

Kawabata A and Kuroda R (2000) Protease-activated receptor (PAR), a novel family of G protein-coupled seven trans-membrane domain receptors: activation mechanisms and physiological roles. *Jpn J Pharmacol* **82**:171–174.

Kawabata A, Kuroda R, Nishida M, Nagata N, Sakaguchi Y, Kawao N, Nishikawa H, Arizono N, and Kawai K (2002b) Protease-activated receptor-2 (PAR-2) in the pancreas and parotid gland: immunolocalization and involvement of nitric oxide in the evoked amylase secretion. *Life Sci* **71**:2435–2446.

Kawabata A, Morimoto N, Nishikawa H, Kuroda R, Oda Y, and Kakehi K (2000a) Activation of protease-activated receptor-2 (PAR-2) triggers mucin secretion in the rat sublingual gland. *Biochem Biophys Res Commun* **270**:298–302.

Kawabata A, Nakaya Y, Ishiki T, Kubo S, Kuroda R, Sekiguchi F, Kawao N, Nishikawa H, and Kawai K (2004b) Receptor-activating peptides for PAR-1 and PAR-2 relax rat gastric artery via multiple mechanisms. *Life Sci* **75**:2689–2702.

Kawabata A, Nishikawa H, Kuroda R, Kawai K, and Hollenberg MD (2000b) Proteinase-activated receptor-2 (PAR-2): regulation of salivary and pancreatic exocrine secretion in vivo in rats and mice. *Br J Pharmacol* **129**:1808–1814.

Kawagoe J, Takizawa T, Matsumoto J, Tamiya M, Meek SE, Smith AJ, Hunter GD, Plevin R, Saito N, Kanke T, et al. (2002) Effect of protease-activated receptor-2 deficiency on allergic dermatitis in the mouse ear. *Jpn J Pharmacol* **88**:77–84.

Koshikawa N, Nagashima Y, Miyagi Y, Mizushima H, Yanoma S, Yasumitsu H, and Miyazaki K (1997) Expression of trypsin in vascular endothelial cells. *FEBS Lett* **409**:442–448.

Lerner DJ, Chen M, Tram T, and Coughlin SR (1996) Agonist recognition by proteinase-activated receptor 2 and thrombin receptor. Importance of extracellular loop interactions for receptor function. *J Biol Chem* **271**:13943–13947.

Macfarlane SR, Seatter MJ, Kanke T, Hunter GD, and Plevin R (2001) Proteinase-activated receptors. *Pharmacol Rev* **53**:245–282.

Maeda A, Kubo T, Mishina M, and Numa S (1988) Tissue distribution of mRNAs encoding muscarinic acetylcholine receptor subtypes. *FEBS Lett* **239**:339–342.

Matsui M, Motomura D, Karasawa H, Fujikawa T, Jiang J, Komiya Y, Takahashi S, and Taketo MM (2000) Multiple functional defects in peripheral autonomic organs in mice lacking muscarinic acetylcholine receptor gene for the M3 subtype. *Proc Natl Acad Sci USA* **97**:9579–9584.

Molino M, Barnathan ES, Numerof R, Clark J, Dreyer M, Cumashi A, Hoxie JA, Schechter N, Woolkalis M, and Brass LF (1997) Interactions of mast cell tryptase with thrombin receptors and PAR-2. *J Biol Chem* **272**:4043–4049.

Mule F, Baffi MC, Falzone M, and Cerra MC (2002) Signal transduction pathways involved in the mechanical responses to protease-activated receptors in rat colon. *J Pharmacol Exp Ther* **303**:1265–1272.

Nagaraju K, Cox A, Casciola-Rosen L, and Rosen A (2001) Novel fragments of the Sjogren's syndrome autoantigens alpha-fodrin and type 3 muscarinic acetylcholine receptor generated during cytotoxic lymphocyte granule-induced cell death. *Arthritis Rheum* **44**:2376–2386.

Nakamura T, Matsui M, Uchida K, Futatsugi A, Kusakawa S, Matsumoto N, Nakamura K, Manabe T, Taketo MM, and Mikoshiba K (2004) M_3 muscarinic acetylcholine receptor plays a critical role in parasympathetic control of salivation in mice. *J Physiol (Lond)* **558**:561–575.

Nystedt S, Emilsson K, Wahlestedt C, and Sundelin J (1994) Molecular cloning of a potential proteinase activated receptor. *Proc Natl Acad Sci USA* **91**:9208–9212.

Ohno-Shosaku T, Matsui M, Fukudome Y, Shosaku J, Tsubokawa H, Taketo MM, Manabe T, and Kano M (2003) Postsynaptic M1 and M3 receptors are responsible for the muscarinic enhancement of retrograde endocannabinoid signalling in the hippocampus. *Eur J Neurosci* **18**:109–116.

Oshiro A, Otani H, Yagi Y, Fukuhara S, and Inagaki C (2002) Protease-activated receptor-2-mediated Ca^{2+} signaling in guinea pig tracheal epithelial cells. *Life Sci* **71**:547–558.

Rose K, Allan A, Gauldie S, Stapleton G, Dobbie L, Dott K, Martin C, Wang L, Hedlund E, Seckl JR, et al. (2001) Neurosteroid hydroxylase CYP7B: vivid reporter activity in dentate gyrus of gene-targeted mice and abolition of a widespread pathway of steroid and oxysterol hydroxylation. *J Biol Chem* **276**:23937–23944.

Slomiany BL, Sengupta S, Piotrowski E, Lopez RA, and Slomiany A (1992) Role of adrenergic and cholinergic mediators in salivary phospholipids secretion. *Biochim Biophys Acta* **1124**:171–177.

Takuma T, Ichida T, and Kumegawa M (1985) Regulation of functional mRNA levels for trypsin-like esteroproteases by 5 alpha-dihydrotestosterone and triiodothyronine in mouse submandibular salivary gland. *Arch Oral Biol* **30**:727–730.

Takuma T and Kumegawa M (1981) Postnatal development of trypsin-like esteroproteases in mouse submandibular gland. *Histochemistry* **72**:25–31.

Wiseman LR and Faulds D (1995) Oral pilocarpine: a review of its pharmacological properties and clinical potential in xerostomia. *Drugs* **49**:143–155.

Address correspondence to: Dr. Ichiro Saito, Department of Pathology, Tsurumi University School of Dental Medicine, 2-1-3 Tsurumi, Tsurumi-ku, Yokohama, 230-8501, Japan. E-mail: saito-i@tsurumi-u.ac.jp

Noninvasive Interference Tear Meniscometry in Dry Eye Patients With Sjögren Syndrome

ATSURO UCHIDA, MIKI UCHINO, EIKI GOTO, ERI HOSAKA, YUKO KASUYA, KAZUMI FUKAGAWA, MURAT DOGRU, YOKO OGAWA, AND KAZUO TSUBOTA

• PURPOSE: To compare noninvasive tear meniscus height (NI-TMH) using a tear interference device in normal subjects and dry eye patients with Sjögren syndrome (SS), and to investigate the applicability of this new method before and after the punctal occlusion procedure.
• DESIGN: Prospective case control study.
• METHODS: Tear meniscus was visualized noninvasively using a tear interference device (Tearscope plus, Keeler, Windsor, United Kingdom). Tear interference image was captured with digital video camera (SP-321, JFC Sales Plan Co, Tokyo, Japan) attached to the slit-lamp. Lower lid margin NI-TMH was measured using image analysis software. NI-TMH of 28 eyes from 17 normal subjects and 46 eyes from 27 aqueous tear deficiency (ATD) dry eye patients with SS were compared. The change of NI-TMH three weeks after the successful punctal occlusion was examined in 11 eyes of eight dry eye subjects.
• RESULTS: Tear meniscus was well visualized with the tear interference device in all cases. Lower lid margin NI-TMH was 0.22 ± 0.065 mm in normal subjects, and 0.13 ± 0.042 mm in SS subjects, respectively ($P < .0001$). After the punctal occlusion, lower lid margin NI-TMH increased significantly from 0.12 ± 0.026 mm to 0.42 ± 0.21 mm ($P = .001$).
• CONCLUSIONS: NI-TMH was substantially lower in SS subjects and also significantly improved after punctal occlusion. This method is expected to be helpful in the diagnosis and in the evaluation of the efficacy of punctal occlusion in ATD dry eyes such as SS. (Am J Ophthalmol 2007;144:232–237. © 2007 by Elsevier Inc. All rights reserved.)

TEARS ARE SECRETED FROM THE LACRIMAL GLAND and distributed by blinking to form the tear film of the ocular surface.[1–3] Tear film is responsible for wetting the ocular surface, which is the first line of defense, and is also essential for clear visual imaging.[4–6] Tears are distributed to the cul-de-sac and the exposed ocular surface area, including tear menisci.[7] Tear meniscus is a major part of the tear reservoir, which holds approximately 70% to 80% of the total tear volume of the exposed ocular surface area. Thus, tear menisci have been considered to reflect tear volume on the ocular surface, and have been considered to be important in the diagnosis of dry eye syndrome.[8]

Using a minimal amount of fluorescein staining, Mainstone and associates reported that the fluorescein-stained tear meniscus height (f-TMH) of normal subjects was 0.46 mm, and f-TMH of dry eye subjects was significantly decreased as 0.24 mm.[9] This conventional method is widely used as the most common method of tear meniscus height (TMH) measurement. Oguz and associates also reported that f-TMH of dry eye subjects using minimal fluorescein was 0.21 mm, and TMH of the same subjects measured by a noninvasive method with slit-lamp equipped with a micrometer-scale was 0.19 mm.[10] In the meantime, they pointed out that TMH of dry eye subjects sometimes could not be observed without fluorescein, since it was too low. Conventional f-TMH has been reported to be of value in the diagnosis of dry eye; however, it was limited by its invasive nature.[9,11–15]

Another method to visualize the lucent tear meniscus is to use interference phenomena. Tear interferometry is a noninvasive visualization method of the lucent tear film. The optical path difference from the reflectance at the surface of the tear lipid layer and at the interface of the tear lipid-aqueous layer causes a tear interference image, which could be clearly observed.[16–18] It has been mainly used to observe the precorneal tear lipid layer.[19–21]

In ophthalmic practice using the tear interference device (Tearscope Plus, Keeler, Windsor, United Kingdom),[22–26] not only can the precorneal tear film be observed clearly and noninvasively, but the tear film at the tear meniscus as well. Therefore, we hypothesized that noninvasive tear meniscus height (NI-TMH) could be quantified with the image analysis of tear meniscus interference image, and could be used to differentiate aqueous tear deficiency (ATD) dry eye such as Sjögren syndrome (SS) or to assess surgical efficacy after dry eye treatment by punctal occlusion. The significance of this method and findings are further discussed.

Accepted for publication Apr 4, 2007.

From the Department of Ophthalmology, School of Medicine, Keio University, Tokyo, Japan (A.U., M.U., E.G., E.H., K.F., M.D., Y.O., K.T.); the Tokyo Dry Eye Center in Iidabashi Eye Clinic, Tokyo, Japan (M.U., K.F.); the Department of Ophthalmology, School of Dental Medicine, Tsurumi University, Yokohama, Japan (E.G., E.H., Y.K.); and the Department of Ophthalmology, Ichikawa General Hospital, Tokyo Dental College, Chiba, Japan (M.D., K.T.).

Inquiries to Eiki Goto, Department of Ophthalmology, School of Dental Medicine, Tsurumi University, 2-1-3 Tsurumi, Tsurumi-ku, Yokohama City, Kanagawa, Japan 230-8501; e-mail: goto-e@tsurumi-u.ac.jp

0002-9394/07/$32.00
doi:10.1016/j.ajo.2007.04.006

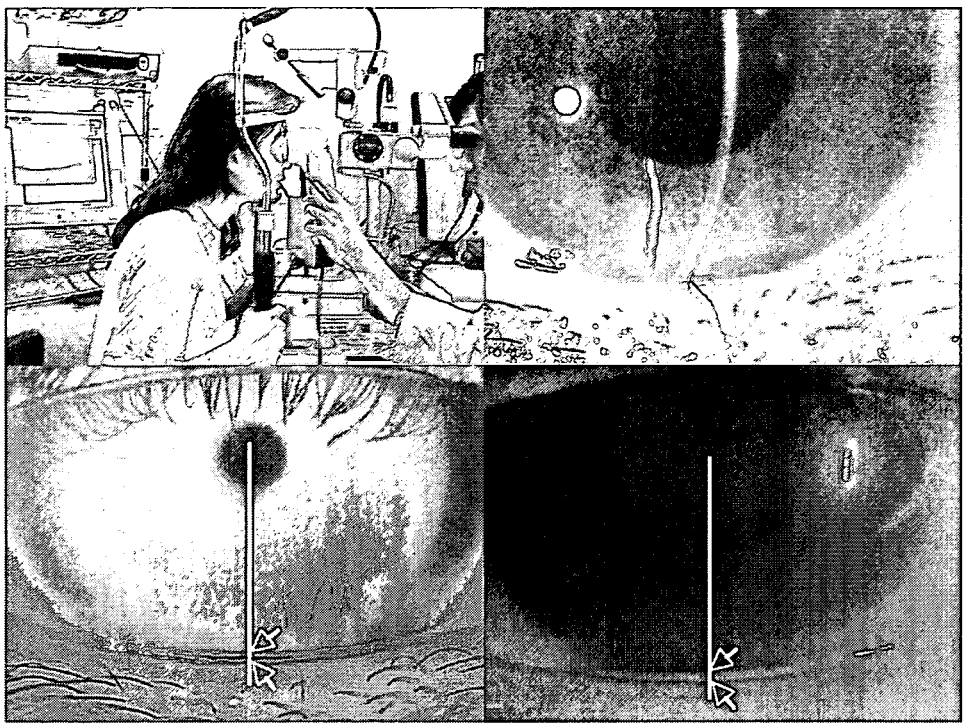

FIGURE 1. Measurement of noninvasive tear meniscus height (NI-TMH) using Tearscope Plus. (Top left) Tearscope interference device is set between the subject's eye and the slit-lamp. Precorneal tear interference image and tear meniscus interference image could be observed through the slit-lamp, and was recorded to the computer through the mounted digital video camera. Tear interference image with meniscus could also be seen on the computer screen. (Top right) Slit-lamp image of tear meniscus with diffuser light is shown. Tear meniscus of the same subject in Top left image is noninvasively visualized (Bottom left) and is also visualized with fluorescein staining (Bottom right). (Bottom left) Using image analysis software, the height of noninvasively visualized tear meniscus (between upper and lower white arrow) in central area (vertical white line) was measured. NI-TMH was quantified as 0.21 mm. Note that surface lipid layer of both tear meniscus and precorneal tear film is visualized by the tear interference device. (Bottom right) Using image analysis software, the height of fluorescein stained tear meniscus (between upper and lower white arrow) in central area (vertical white line) was measured in the same image capturing system. Fluorescein-stained tear meniscus height was quantified as 0.24 mm.

METHODS

• MEASUREMENT OF NONINVASIVE TEAR MENISCUS HEIGHT USING TEAR INTERFERENCE DEVICE: Tearscope Plus tear interference device was attached to the slit-lamp (SL130, Zeiss, Jena, Germany, magnification fixed to 12 ×, Figure 1). The tear interference image of the lower tear meniscus could be observed noninvasively when focusing at the lower lid margin. The image was captured using a high quality digital video camera (SP-321, JFC Sales Plan Co, Tokyo, Japan) attached through the beam-splitter of the slit-lamp and recorded using an image capturing system (P4m/MaxFile, P4 Medic Co, Kobe, Japan) in 720 × 480 pixels sized JPEG format. NI-TMH was measured using the ImageJ 1.32 image analysis software (National Institutes of Health, Bethesda, Maryland, USA). None of the subjects received any eye drop instillations at least six hours before the measurement.

As NI-TMH measurement with Tearscope Plus device has not been reported, it was compared concomitantly with conventional f-TMH in 31 eyes of 16 subjects. Nine eyes of five dry eye patients with SS (five females, mean age, 64 ± 8 years) and 22 eyes of 11 normal subjects (five males and six females, mean age, 34 ± 12 years) were measured. Initially, NI-TMH was measured with the Tearscope Plus tear interference device. Then, f-TMH was measured one minute after instillation of 2 μl of fluorescein solution with a micropipette. The images of NI-TMH and f-TMH were recorded and measured using exactly the same set-up as described above. The mean NI-TMH was 0.20 ± 0.09 mm, and f-TMH was 0.26 ± 0.11 mm. Images of the representative cases of NI-TMH and f-TMH are shown in Figure 1. The correlation between NI-TMH and f-TMH was also calculated with linear regression analysis. A significant correlation was found between NI-TMH and f-TMH ($r = .79$, $P < .0001$).

• SUBJECTS AND ASSESSMENT OF TEARS AND OCULAR SURFACE: We examined a consecutive series of 27 dry eye patients with SS (46 eyes, all female, mean age, 62 ± 10 years), as well as 17 normal subjects (28 eyes, all female, mean age, 52 ± 16 years). SS patients were diagnosed

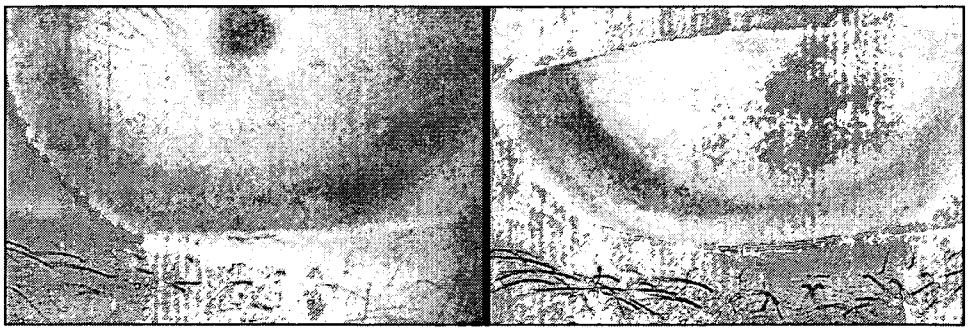

FIGURE 2. Noninvasive tear meniscus height (NI-TMH) between normal subjects and dry eye with Sjögren syndrome (SS). (Left) NI-TMH of a representative normal subject (0.28 mm). (Right) NI-TMH of a representative dry eye subject with SS (0.094 mm).

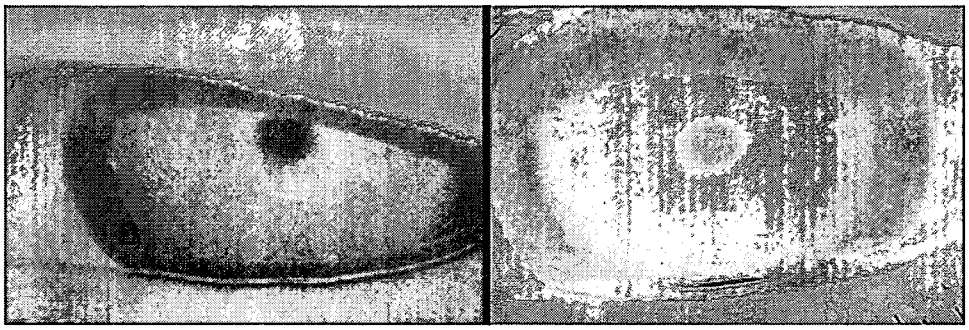

FIGURE 3. Noninvasive tear meniscus height (NI-TMH) before and after punctal occlusion. (Left) NI-TMH of a representative dry eye patient with Sjögren syndrome (SS) before punctal occlusion (0.17 mm). (Right) NI-TMH after punctual occlusion of the same patient (0.56 mm).

according to the criteria of Fox and associates.[27] Among the SS patients, eyes with a Schirmer I test value less than or equal to 5 mm were included in the study as they were considered to have ATD dry eye according to the Japanese dry eye criteria.[28] Eyes with a history of punctal occlusion, conjunctivochalasis, corneal transplantation, or corneal perforation were excluded from the study. In addition, eyes with anterior blepharitis and infectious conjunctivitis were also excluded. No patients used contact lenses in this study.

NI-TMH was assessed as described above before any invasive procedure. After that, the cornea was examined by fluorescein staining. A 2-μl volume of preservative-free solution consisting of 1% fluorescein dye was applied to the conjunctival sac. The intensity of the actual fluorescein staining of the cornea such as superficial punctate keratopathy was rated from a minimum of zero to a maximum of three, in each upper, middle, and lower cornea. Thus, the maximum total staining score was 9.[29] Tear film break-up time (BUT) was measured three times, and the measurements were averaged.[29] 2 μl of preservative-free solution consisting of 1% Rose Bengal dye was then applied to the conjunctival sac. The intensity of rose bengal staining in the cornea and conjunctiva was recorded, with the maximum score rated as nine points.[30] The Schirmer I test was then performed to measure the tear secretion volume.[31] NI-TMH was compared between dry eye subjects and normal controls.

• CHANGE OF TEAR MENISCUS HEIGHT AFTER PUNCTAL OCCLUSION: All dry eye patients received treatment with non-preserved artificial tears, and 0.1% non-preserved hyaluronic acid eye drops as necessary for at least two months. These subjects who were refractory to this treatment protocol underwent punctal occlusion. NI-TMH was compared before and three weeks after punctal occlusion or punctal plug insertion for both superior and inferior puncta in 11 eyes of eight subjects in an additional interventional case series (eight females, mean age, 69 ± 8 years). Flex plugs (Eagle Vision, Memphis, Tennessee, USA) were used for punctal occlusion in three eyes of three subjects, and punctal cauterization using Optemp 2 (Alcon, Fort Worth, Texas, USA) was performed in eight eyes of five subjects. Tseng's method was performed in punctal occlusion surgery[32] and the operation was successful in all cases without re-canalization.

• STATISTICAL ANALYSIS: All data are shown as means ± standard deviation. The Mann-Whitney *U* test was applied to the comparison of NI-TMH, fluorescein staining, rose bengal staining, tear film BUT, and Schirmer I test between SS and normal subjects. Wilcoxon matched pairs

test was applied to the comparison before and after punctal occlusion at each examination. A level of $P < .05$ was accepted as statistically significant. Graphpad Instat 3.0 (Graphpad Software Inc, San Diego, California, USA) was used for statistical analysis.

RESULTS

THE MEAN NI-TMH IN NORMAL SUBJECTS WAS 0.22 ± 0.065 mm. On the contrary, it was significantly lower (0.13 ± 0.042 mm, $P < .0001$) in dry eye patients with SS. The representative cases are shown in Figure 2. Corneal fluorescein staining mean score was significantly lower (0.46 ± 0.64) in normal subjects compared to dry eye patients with SS (4.0 ± 2.1, $P < .0001$). Rose Bengal staining mean score was significantly lower in normal subjects (0.18 ± 0.48) compared to dry eye patients with SS (4.6 ± 1.8, $P < .0001$). Similarly, tear film BUT was 5.9 ± 3.0 seconds in normal subjects, and it was significantly longer than in dry eye patients with SS (2.3 ± 1.4 seconds, $P < .0001$). Schirmer I test result was 13.9 ± 9.4 mm in normal subjects, and it was significantly longer than in dry eye patients with SS (1.7 ± 1.5 mm, $P < .0001$).

Images of NI-TMH before and after punctal occlusion in the representative case are shown in Figure 3. The mean NI-TMH significantly increased from 0.12 ± 0.026 mm to 0.42 ± 0.21 mm after the punctal occlusion procedure ($P = .001$). NI-TMH was increased after both punctal cauterization or punctal plug insertion procedures. In addition, corneal fluorescein staining mean score significantly decreased from 4.5 ± 2.3 to 0.27 ± 0.65 ($P = .002$), tear film BUT was prolonged from 0.91 ± 0.30 seconds to 5.2 ± 2.8 seconds ($P = .001$) and the Schirmer I test result increased from 2.8 ± 2.0 mm to 6.8 ± 4.2 mm ($P = .005$). On the contrary, Rose Bengal staining mean score decreased, but not significantly, from 5.0 ± 1.7 to 2.5 ± 2.0 ($P = .06$).

DISCUSSION

IN THE PRESENT STUDY, USING THE TEAR INTERFERENCE device, tear meniscus was successfully visualized in a noninvasive manner in all cases. We showed that NI-TMH measurement could be as relevant as the conventional f-TMH measuring method in the diagnosis of dry eye syndromes, could differentiate between normal subjects and ATD dry eye patients with SS, and could help in the evaluation of the change of meniscus height after punctal occlusion.

NI-TMH was significantly lower in dry eye patients with SS (0.13 ± 0.042 mm) compared with normal controls, (0.22 ± 0.065 mm) along with higher fluorescein and rose bengal staining, shortened tear film BUT, and lower Schirmer I test result. After punctal occlusion, NI-TMH significantly increased from 0.12 ± 0.026 mm to 0.42 ± 0.21 mm along with the improvement of corneal fluorescein staining, tear film BUT, and Schirmer I test result. NI-TMH was increased after both punctal cauterization or punctal plug insertion procedures. We believe that NI-TMH accurately reflects the deficiency of tear volume on the ocular surface in ATD dry eye patients with SS.

The values of NI-TMH in this study are low compared with the previous studies on TMH.[9,11–15,33] The previous data related to TMH mainly measured with fluorescein dye. In this study, a significant correlation was found between NI-TMH and f-TMH, and NI-TMH was slightly lower than f-TMH. This was possibly because of the addition of a minimal amount of water added to the fluorescein dye. The other merit of the present method is visualization ability even when the TMH is very low. In a previous study, using direct observation of the TMH with the slit-lamp, Oguz and associates reported that tear meniscus could not be observed when it was too low in dry eye subjects.[10] Our method using interference phenomena could visualize clearly such low tear meniscus even in ATD dry eyes with SS (Figures 2 and 3). Furthermore, in the principle of tear interferometry, reflectance is ranged approximately from 2% to 6%.[17,18,34] Thus, tear interference image of tear meniscus could be visualized even in dry eye cases with lipid tear deficiency. Using optical coherence tomography in ATD dry eyes, Savini and associates recently reported that mean NI-TMH was significantly lower in patients with ATD dry eyes (0.13 ± 0.07 mm) than in the control group (0.25 ± 0.08 mm).[35] We considered that their results strongly support the relevance of our method.

Compared with fluorescein-stained tear meniscus observation, noninvasive tear meniscus observation using the interference device has one demerit in terms of the limitation in the observation area. As shown in the figures, this method could visualize frontal tear meniscus at a limited observation angle. To observe all lower and upper tear meniscus areas from the inner to outer canthi, we considered that the fluorescein staining method still has some advantages.

Recently, another tear meniscus measuring device to measure meniscus radius curvature has been reported by Yokoi and associates.[36,37] This noninvasive method, however, is not widely available yet, and we chose the Tearscope interference device for the evaluation of tear meniscus in this study. Furthermore, height and radius of tear meniscus have been reported to have a positive correlation by Yokoi's group.[10] Thus, we also believe that the measurement of the NI-TMH is important, as well as tear meniscus radius measurement.[38]

In this study, we compared NI-TMH of normal and dry eye patients with SS who are representing ATD dry eyes. In the future, NI-TMH measurement of the other dry eye subtypes such as non-SS dry eye, meibomian gland dys-

function,[39] or dry eye with only decreased tear film BUT[40] would be highly anticipated. Furthermore, observation of the upper NI-TMH using Tearscope in superior limbic keratoconjunctivitis,[41] or lid-wiper syndrome[42] would be also interesting.

As many clinicians are aware, the diagnosis of ATD dry eyes is sometimes difficult owing to the variability of the Schirmer I test results by its invasive nature. In the future, we expect that NI-TMH measurement by the tear interference device would become an established tear volume evaluation test such as the Schirmer I test.[31]

In conclusion, NI-TMH measurement using the tear interference device could be considered to have similar clinical relevance compared with conventional f-TMH measurement. Not only did this method evaluate tear aqueous volume noninvasively, but it could also indicate significantly lower NI-TMH in ATD dry eye patients with SS and, was useful for indicating the increase of NI-TMH after the punctal occlusion procedure. The difference of NI-TMH in normal and dry eye groups was considered to reflect the difference of tear volume, which is responsible for moistening and maintaining the ocular surface.

THIS STUDY WAS SUPPORTED BY GRANT NO. 18070501 FROM THE JAPANESE MINISTRY OF HEALTH, LABOUR, AND WELFARE, Tokyo, Japan. The authors indicate no financial conflict of interest. Involved in design of study (A.U., M.U., E.G.); conduct of study (E.G., K.F., M.D., Y.O., K.T.); collection and analysis of the data (A.U., M.U., E.G., E.H., Y.K.); and approval of the manuscript (E.G., M.D., Y.O., K.T.). Drs Uchida, Uchino, and Goto contributed equally to this study and therefore should be considered equivalent first authors. This research followed the Tenets of the Declaration of Helsinki and informed consent was obtained from all the subjects after explanation of the nature and possible consequences of the study. Institutional Review Board (IRB) committee approval was obtained at Tsurumi University. This clinical trial was registered to Japan Pharmaceutical Information Center, Tokyo, Japan, JapacCTI-060313.

The authors would like to thank Y. Yamamoto, MD, Y. Tatematsu, MD, E. Sugisaka, MD, R. Nishimura, MD, K. Hashizume, MD, and T. Yamaguchi, MD, from the Department of Ophthalmology, School of Medicine, Keio University, Tokyo, Japan for assisting with data acquisition.

REFERENCES

1. Lemp MA. Report of the National Eye Institute/Industry workshop on Clinical Trials in Dry Eyes. CLAO J 1995;21: 221–232.
2. Lemp MA. Epidemiology and classification of dry eye. Adv Exp Med Biol 1998;438:791–803.
3. Pflugfelder SC, Tseng SCG, Sanabria O, et al. Evaluation of subjective assessments and objective diagnostic tests for diagnosing tear-film disorders known to cause ocular irritation. Cornea 1998;17:38–56.
4. Rieger G. The importance of the precorneal tear-film for the quality of optical imaging. Br J Ophthalmol 1992;76:157–158.
5. Goto E, Yagi Y, Matsumoto Y, Tsubota K. Impaired functional visual acuity of dry eye patients. Am J Ophthalmol 2002;133:181–186.
6. Goto E, Yagi Y, Kaido M, Matsumoto Y, Konomi K, Tsubota K. Improved functional visual acuity after punctal occlusion in dry eye patients. Am J Ophthalmol 2003;135:704–705.
7. Mishima S, Gasset A, Klyce SD, Jr, Baum JL. Determination of tear volume and tear flow. Invest Ophthalmol 1966;5: 264–276.
8. Dogru M, Ishida K, Matsumoto Y, et al. Strip meniscometry: a new and simple method of tear meniscus evaluation. Invest Ophthalmol Vis Sci 2006;47:1895–1901.
9. Mainstone JC, Bruce AS, Golding TR. Tear meniscus measurement in the diagnosis of dry eye. Curr Eye Res 1996;15:653–661.
10. Oguz H, Yokoi N, Kinoshita S. The height and radius of the tear meniscus and methods for examining these parameters. Cornea 2000;19:497–500.
11. Scherz W, Doane MG, Dohlman CH. Tear volume in normal eyes and keratoconjunctivitis sicca. Albrecht von Graefes Arch Klin Exp Ophthalmol 1974;192:141–150.
12. McDonald JE, Brubaker S. Meniscus-induced thinning of tear-films. Am J Ophthalmol 1971;72:139–146.
13. Golding TR, Bruce AS, Mainstone JC. Relationship between tear-meniscus parameters and tear-film breakup. Cornea 1997;16:649–661.
14. Holly FJ. Physical chemistry of the normal and disordered tear-film. Trans Ophthalmol Soc U K 1985;104:374–380.
15. Holly FJ. Tear physiology and dry eyes. Surv Ophthalmol 1977;22:69–87.
16. Guenther R. Interference. Modern Optics. New York, New York: Wiley, 1990:87–128.
17. Goto E, Dogru M, Kojima T, Tsubota K. Computer synthesis of an interference color chart of human tear lipid layer, by a colorimetric approach. Invest Ophthalmol Vis Sci 2003;44: 4693–4697.
18. King-Smith PE, Fink BA, Fogt N. Three interferometric methods for measuring the thickness of layers of the tear-film. Optom Vis Sci 1999;76:19–32.
19. Goto E, Dogru M, Fukagawa K, et al. Successful tear lipid layer treatment for refractory dry eye in office workers by low-dose lipid application on the full-length eyelid margin. Am J Ophthalmol 2006;142:264–270.
20. Norn MS. Semiquantitative interference study of fatty layer of precorneal film. Acta Ophthalmol (Copenh) 1979;57: 766–774.
21. Yokoi N, Takehisa Y, Kinoshita S. Correlation of tear lipid layer interference patterns with the diagnosis and severity of dry eye. Am J Ophthalmol 1996;122:818–824.
22. Isenberg SJ, Del Signore M, Chen A, Wei J, Guillon JP. The lipid layer and stability of the preocular tear-film in newborns and infants. Ophthalmology 2003;110:1408–1411.
23. Nichols JJ, Nichols KK, Puent B, Saracino M, Mitchell GL. Evaluation of tear-film interference patterns and measures of tear break-up time. Optom Vis Sci 2002;79:363–369.
24. Tomlinson A, Pearce EI, Simmons PA, Blades K. Effect of oral contraceptives on tear physiology. Ophthalmic Physiol Opt 2001;21:9–16.
25. Guillon M, Styles E, Guillon JP, Maissa C. Preocular tear-film characteristics of nonwearers and soft contact lens wearers. Optom Vis Sci 1997;74:273–279.

26. Craig JP, Tomlinson A. Importance of the lipid layer in human tear-film stability and evaporation. Optom Vis Sci 1997;74:8–13.
27. Fox RI, Robinson CA, Curd JG, Kozin F, Howell FV. Sjögren's syndrome. Proposed criteria for classification. Arthritis Rheum 1986;29:577–585.
28. Danjo Y. Diagnostic usefulness and cutoff value of Schirmer's I test in the Japanese diagnostic criteria of dry eye. Graefes Arch Clin Exp Ophthalmol 1997;235:761–766.
29. Toda I, Tsubota K. Practical double vital staining for ocular surface evaluation. Cornea 1993;12:366–367.
30. van Bijsterveld OP. Diagnostic tests in the Sicca syndrome. Arch Ophthalmol 1969;82:10–14.
31. Schirmer O. Studien zur physiologie und pathologie der tranenabsonderung und tranenabfuhr. Albrebt von Graefes Archiv fur Ophthalmologie 1903;56:197–291.
32. Goto E, Tseng SC. Kinetic analysis of tear interference images in aqueous tear deficiency dry eye before and after punctal occlusion. Invest Ophthalmol Vis Sci 2003;44:1897–1905.
33. Johnson ME, Murphy PJ. The agreement and repeatability of tear meniscus height measurement methods. Optom Vis Sci 2005;82:1030–1037.
34. Goto E, Tseng SC. Differentiation of lipid tear deficiency dry eye by kinetic analysis of tear interference images. Arch Ophthalmol 2003;121:173–180.
35. Savini G, Barboni P, Zanini M. Tear meniscus evaluation by optical coherence tomography. Ophthalmic Surg Lasers Imaging 2006;37:112–118.
36. Yokoi N, Bron A, Tiffany J, Brown N, Hsuan J, Fowler C. Reflective meniscometry: a non-invasive method to measure tear meniscus curvature. Br J Ophthalmol 1999;83:92–97.
37. Yokoi N, Bron AJ, Tiffany JM, Maruyama K, Komuro A, Kinoshita S. Relationship between tear volume and tear meniscus curvature. Arch Ophthalmol 2004;122:1265–1269.
38. Creech JL, Do LT, Fatt I, Radke CJ. In vivo tear-film thickness determination and implications for tear-film stability. Curr Eye Res 1998;17:1058–1066.
39. Goto E, Shimazaki J, Monden Y, et al. Low-concentration homogenized castor oil eye drops for noninflamed obstructive meibomian gland dysfunction. Ophthalmology 2002;109:2030–2035.
40. Toda I, Shimazaki J, Tsubota K. Dry eye with only decreased tear break-up time is sometimes associated with allergic conjunctivitis. Ophthalmology 1995;102:302–309.
41. Goto E, Shimmura S, Shimazaki J, Tsubota K. Treatment of superior limbic keratoconjunctivitis by application of autologous serum. Cornea 2001;20:807–810.
42. Korb DR, Greiner JV, Herman JP, et al. Lid-wiper epitheliopathy and dry-eye symptoms in contact lens wearers. CLAO J 2002;28:211–216.

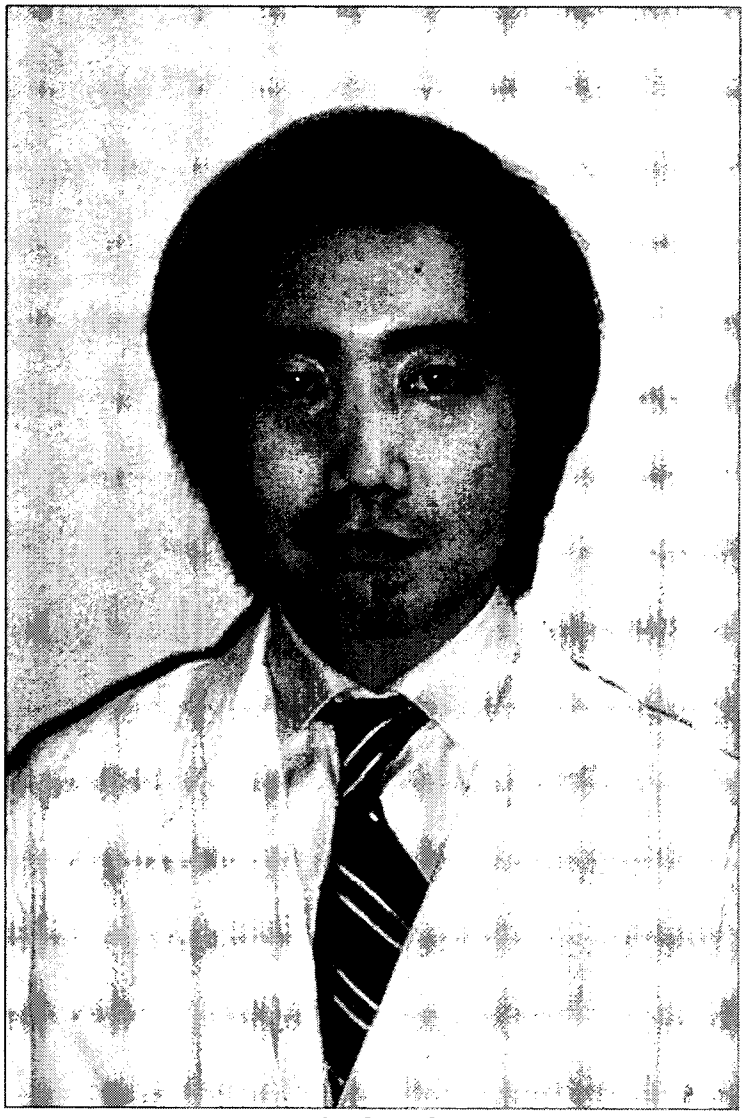

Biosketch

Atsuro Uchida, MD, graduated from Keio University School of Medicine, Tokyo, Japan, in 2001, and served as an ophthalmologist at Keio University Hospital and Keiyu Hospital, Yokohama, Japan from 2001 to 2007. Dr Uchida is affiliated with Japanese Ophthalmological Society and the Association for Research in Vision and Ophthalmology. Dr Uchida's primary research interests are dry eye and tear meniscus.

Vol 441|15 June 2006|doi:10.1038/nature04724

nature

LETTERS

Suppression of basal autophagy in neural cells causes neurodegenerative disease in mice

Taichi Hara[1], Kenji Nakamura[2], Makoto Matsui[1,3,4], Akitsugu Yamamoto[5], Yohko Nakahara[2], Rika Suzuki-Migishima[2], Minesuke Yokoyama[6], Kenji Mishima[7], Ichiro Saito[7], Hideyuki Okano[8,9] & Noboru Mizushima[1,10]

Autophagy is an intracellular bulk degradation process through which a portion of the cytoplasm is delivered to lysosomes to be degraded[1–4]. Although the primary role of autophagy in many organisms is in adaptation to starvation, autophagy is also thought to be important for normal turnover of cytoplasmic contents, particularly in quiescent cells such as neurons. Autophagy may have a protective role against the development of a number of neurodegenerative diseases[5–8]. Here we report that loss of autophagy causes neurodegeneration even in the absence of any disease-associated mutant proteins. Mice deficient for *Atg5* (autophagy-related 5) specifically in neural cells develop progressive deficits in motor function that are accompanied by the accumulation of cytoplasmic inclusion bodies in neurons. In $Atg5^{-/-}$ cells, diffuse, abnormal intracellular proteins accumulate, and then form aggregates and inclusions. These results suggest that the continuous clearance of diffuse cytosolic proteins through basal autophagy is important for preventing the accumulation of abnormal proteins, which can disrupt neural function and ultimately lead to neurodegeneration.

Every eukaryotic cell has two main systems for the degradation of intracellular components: the ubiquitin–proteasome system and autophagy. Autophagy is a generic term for the degradation of cellular components in lysosomes[1–4]. Macroautophagy (hereafter referred to as autophagy) is believed to be the main pathway among several subtypes of autophagy. During the process of autophagy, small portions of cytoplasm are sequestered by autophagosomes and then degraded on fusion with lysosomes. In contrast to the ubiquitin–proteasome system, which accounts for most of the selective intracellular protein degradation, autophagy is less selective. Autophagy induced by starvation is a mechanism for producing amino acids within cells. In yeast, autophagy-defective cells are susceptible to starvation. In comparison, mice deficient for Atg5 and Atg7, which are essential for autophagosome formation[9], suffer from severe nutrient- and energy-insufficiency soon after birth[10,11]. Thus, adaptation to starvation is an evolutionarily conserved role of autophagy.

In addition to induced autophagy, a low level of constitutive autophagy is important for intracellular clearance under normal conditions. Mice bearing a liver-specific conditional knockout allele of *Atg7* show hepatic dysfunction and intracellular ubiquitin-positive inclusion bodies[11]. We have also observed the accumulation of ubiquitin-positive inclusion bodies in hepatocytes and a subset of neurons in *Atg5*-knockout ($Atg5^{-/-}$) neonates (Supplementary Fig. S1); however, conventional histological analysis revealed no significant abnormality[10]. These data suggest that intracellular protein quality-control by autophagy is particularly important in neural cells. Indeed, several studies have suggested that impairment of autophagy could worsen the accumulation of abnormal proteins in neurodegenerative disease models *in vitro* and *in vivo*[5–8]. However, direct evidence demonstrating that autophagy contributes to the prevention of neurodegeneration has been lacking, in part because $Atg5^{-/-}$ and $Atg7^{-/-}$ mice die soon after birth[10,11].

To determine the role of autophagy in neural cells, we generated neural-cell-specific $Atg5^{-/-}$ mice (Supplementary Fig. S2). Mice bearing an $Atg5^{flox}$ allele, in which exon 3 of the *Atg5* gene is flanked by two *loxP* sequences, were crossed with a transgenic line expressing Cre recombinase under the control of the nestin promoter (nestin-*Cre*)[12]. In these mice, Cre recombinase is expressed in neural precursor cells after embryonic day (E)10.5, causing deletion of the *loxP*-flanked exon 3 (Supplementary Fig. S3). Recombination was successful in over 90% of all brain cells from $Atg5^{flox/flox}$; nestin-*Cre* mice. The expression of Atg5 (detected as an Atg12–Atg5 conjugate[13]) and the Atg5-dependent conversion of microtubule-associated protein 1 light chain 3 (LC3)-I to LC3-II (LC3–phosphatidylethanolamine (LC3–PE) conjugate)[13,14] were almost completely suppressed in the brains of $Atg5^{flox/flox}$; nestin-*Cre* mice after E15.5 (Fig. 1a and Supplementary Fig. S3). These data suggest that autophagosome formation is impaired in the brains of these mutant mice.

$Atg5^{flox/flox}$; nestin-*Cre* mice were born normally and survived neonatal starvation. They did not show the suckling defects observed in $Atg5^{-/-}$ and $Atg7^{-/-}$ neonates[10,11], suggesting that an undetectable, but sufficient, level of Atg5 remains in the neurons controlling the suckling response at this stage, or that non-neural cells may mediate the suckling deficit in the non-conditional mutants. However, the $Atg5^{flox/flox}$; nestin-*Cre* mice showed growth retardation: their mean body weight was about 1.5-times lower than that of control ($Atg5^{flox/+}$; nestin-*Cre*) mice (Fig. 1b). $Atg5^{flox/flox}$; nestin-*Cre* mice developed progressive motor and behavioural deficits after three weeks of age, and footprint analysis revealed an ataxic walking pattern (Fig. 1c). Mean stride lengths corrected for paw base widths were significantly decreased compared with control ($Atg5^{flox/+}$; nestin-*Cre*) mice. The $Atg5^{flox/flox}$; nestin-*Cre* mice showed limb-clasping reflexes when they were suspended by their tails, whereas control mice extended their limbs (Fig. 1d). This abnormal reflex is often observed in mouse models of neurodegenerative disease[15,16].

[1]Department of Bioregulation and Metabolism, Tokyo Metropolitan Institute of Medical Science, Tokyo 113-8613, Japan. [2]Mouse Genome Technology Laboratory, Mitsubishi Kagaku Institute of Life Sciences, Tokyo 194-8511, Japan. [3]Department of Basic Biology, School of Life Science, the Graduate University for Advanced Studies, Okazaki 444-8585, Japan. [4]Department of Cell Biology, National Institute for Basic Biology, Okazaki 444-8585, Japan. [5]Department of Bio-Science, Nagahama Institute of Bio-Science and Technology, Nagahama 526-0829, Japan. [6]Brain Research Institute, Niigata University, Niigata 951-8510, Japan. [7]Department of Pathology, Tsurumi University School of Dental Medicine, Yokohama 230-8501, Japan. [8]Department of Physiology, Keio University School of Medicine, Tokyo 160-8582, Japan. [9]SORST and [10]PRESTO, Japan Science and Technology Agency, Kawaguchi 332-0012, Japan.

Rotarod (Fig. 1e) and wire-hanging (data not shown) tasks also showed severely impaired motor coordination, balance and grip strength in *Atg5*$^{flox/flox}$; nestin-*Cre* mice. Finally, tremor was apparent in 12-week-old mice. Some of the *Atg5*$^{flox/flox}$; nestin-*Cre* mice died after three weeks of age. Neither *Atg5*$^{flox/flox}$ mice (Cre-negative) nor *Atg5*$^{flox/+}$; nestin-*Cre* mice showed any abnormal phenotype.

The gross anatomy of the brain of the mutant mice was normal. However, histological examination revealed degenerative changes in the neurons of *Atg5*$^{flox/flox}$; nestin-*Cre* mice. These alterations were most prominent in cerebellar Purkinje cells. Haematoxylin and eosin (H&E) staining (arrowheads in Fig. 2a) and immunohistochemical staining with an antibody directed against calbindin (a selective marker for Purkinje cells, left panels in Fig. 2b), demonstrated partial loss of these neurons (Fig. 2c). The remaining Purkinje cells showed eccentrically located nuclei, with infolding of the nuclear membrane. We also found a number of eosinophilic spheroids in H&E-stained sections in the cerebellar nuclei of these mutant mice (arrows in Fig. 2a), which probably correspond to the calbindin-positive spheroids in the same region (Fig. 2b, right panels). These structures suggest massive swelling of Purkinje cell axons that project to the cerebellar nuclei[17,18]. In addition, TUNEL-positive cells were detected in the adjacent granular layer, suggesting apoptosis of granular cells in *Atg5*$^{flox/flox}$; nestin-*Cre* mice (Fig. 2d). Consistent with previous observations, the survival of granular cells largely depends on their synaptic connectivity with Purkinje cells[19]. Axonal swelling was observed in other regions of the *Atg5*$^{flox/flox}$; nestin-*Cre* brain, including the cerebral cortex, the nucleus gracilis (Fig. 2a), the posterior thalamic nucleus, hippocampus, inferior colliculus, trigeminal nucleus, parabranchial nucleus, anterior thalamic nucleus, caudal pons and reticular nucleus (data not shown). Partial loss of pyramidal cells also was observed in the cerebral cortex (data not shown). Together, these data suggest that *Atg5*$^{flox/flox}$; nestin-*Cre* mice suffer from neurodegeneration.

We next examined protein aggregation in the brain using an antibody against ubiquitin, a marker of misfolded proteins. Large, ubiquitin-positive inclusion bodies accumulated in the cytoplasm of large neurons in the thalamus, pons, medulla, dorsal root ganglion (DRG) (Fig. 3a) and midbrain (data not shown) of *Atg5*$^{flox/flox}$; nestin-*Cre* mice. Neurons in the cerebral cortex, hippocampus (especially in the CA3 and CA4 regions) (Fig. 3a), striatum and olfactory bulb (data not shown) were also positive for these inclusion

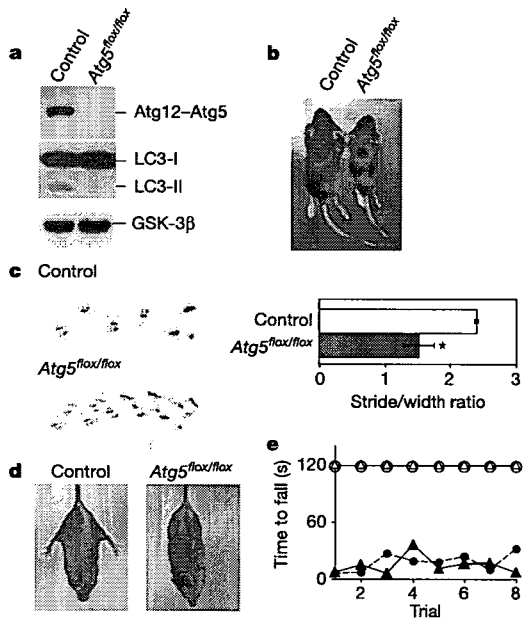

Figure 1 | Behavioural abnormalities in mice lacking *Atg5* in the nervous system. **a**, Immunoblot analysis of Atg5 and LC3. Brain homogenates were prepared from six-week-old control (*Atg5*$^{flox/+}$; nestin-*Cre*) and *Atg5*$^{flox/flox}$; nestin-*Cre* (*Atg5*$^{flox/flox}$) mice. Immunoblot analysis was performed using antibodies against Atg5 and LC3. GSK-3β was used as a loading control. The positions of the Atg12–Atg5 conjugate, LC3-I and LC3-II (LC3–PE conjugate) are indicated. Atg5 monomer was not detected in either lane (data not shown). **b**, A representative male control (*Atg5*$^{flox/+}$; nestin-*Cre*) and an *Atg5*$^{flox/flox}$; nestin-*Cre* (*Atg5*$^{flox/flox}$) littermate at three weeks of age. **c**, Left, paw placement records of eight-week-old mice. Right, stride lengths corrected for paw base widths (stride/width ratio) of *Atg5*$^{flox/flox}$; nestin-*Cre* and control (*Atg5*$^{flox/+}$; nestin-*Cre*) littermate mice. Values represent means ± s.d. of four mice. Asterisk, $P < 0.01$ (Student's *t*-test). **d**, Abnormal limb-clasping of an *Atg5*$^{flox/flox}$; nestin-*Cre* mouse compared with a control mouse (*Atg5*$^{flox/+}$; nestin-*Cre*) when suspended by its tail. **e**, Rotarod testing of *Atg5*$^{flox/+}$; nestin-*Cre* (open symbols) and *Atg5*$^{flox/flox}$; nestin-*Cre* (closed symbols) mice. One male and one female mouse were analysed for each genotype. The time until drop from the rod (rotating at 20 r.p.m.) is shown.

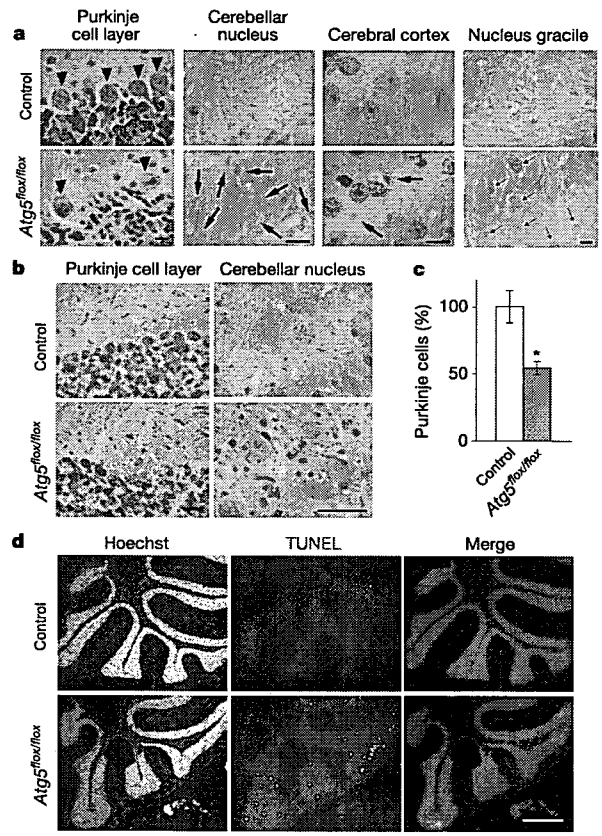

Figure 2 | Neuronal degeneration in *Atg5*$^{flox/flox}$; nestin-*Cre* mice. **a**, H&E-stained sections of the cerebral cortex, the gracile nucleus and cerebellum from control (*Atg5*$^{flox/+}$; nestin-*Cre*) and *Atg5*$^{flox/flox}$; nestin-*Cre* (*Atg5*$^{flox/flox}$) mice at three months of age. Purkinje cells are indicated with arrowheads. Arrows indicate eosinophilic spheroids, which represent axon swelling. Scale bar, 10 μm. **b**, Immunohistochemistry using an anti-calbindin antibody on cerebellum sections from control (*Atg5*$^{flox/+}$; nestin-*Cre*) and *Atg5*$^{flox/flox}$; nestin-*Cre* mice at six weeks of age. Scale bar, 25 μm. **c**, Loss of Purkinje cells in *Atg5*$^{flox/flox}$; nestin-*Cre* mice. Purkinje cells were counted in comparable areas for each mouse, and three fields were counted in each area for each mouse. Data are normalized against values from control mice (*Atg5*$^{flox/+}$; nestin-*Cre*). Values represent mean ± s.d. of three mice. Asterisk, $P < 0.01$ (*t*-test). **d**, Apoptotic death of granular cells. Cerebellum sections from control (*Atg5*$^{flox/+}$; nestin-*Cre*) and *Atg5*$^{flox/flox}$; nestin-*Cre* mice at six weeks of age were subjected to TUNEL staining. Nuclei were stained with Hoechst 33258. Scale bar, 500 μm.

bodies. Such inclusion bodies were not observed in the brains of control (*Atg5*$^{flox/+}$; nestin-*Cre*) mice. We observed ubiquitin-positive inclusion bodies exclusively in cells positive for the neural cell marker NeuN, suggesting that inclusion bodies were generated only in neurons and not in glial cells (Fig. 3b). Notably, although there was extensive loss of Purkinje cells, these neurons had very few inclusion bodies in their cell bodies (Fig. 3a). Numerous ubiquitin-positive dots were observed in the cerebellar nuclei (Fig. 3a), but most of them did not colocalize with the calbindin dots observed in Fig. 2b (data not shown).

The accumulation of inclusion bodies was time-dependent, and the distribution of inclusion-body-positive cells was more limited in *Atg5*$^{-/-}$ and *Atg5*$^{flox/flox}$; nestin-*Cre* newborns compared to adult mice. In *Atg5*$^{-/-}$ neonates, inclusion bodies were observed in the pons, DRG, spinal cord (ventral horn) (Supplementary Fig. S1), hypothalamus, midbrain and trigeminal ganglia (data not shown), but not in the cerebral cortex (Supplementary Fig. S1). A similar pattern was observed in the brain and DRG of *Atg5*$^{flox/flox}$; nestin-*Cre* neonates (Supplementary Fig. S4 and data not shown). Immuno-electron microscopy of DRG neurons isolated from *Atg5*$^{-/-}$ neonates

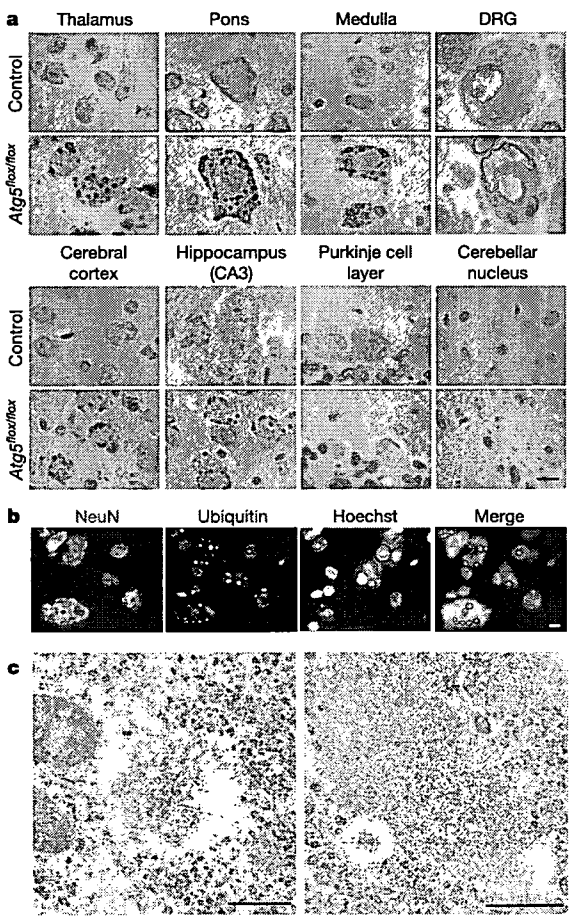

Figure 3 | Ubiquitin-positive inclusions in *Atg5*-deficient neurons. **a**, Immunohistochemistry of brain sections from control (*Atg5*$^{flox/+}$; nestin-*Cre*) and *Atg5*$^{flox/flox}$; nestin-*Cre* (*Atg5*$^{flox/flox}$) mice at six weeks of age, stained with an anti-ubiquitin antibody (1B3). Scale bar, 10 μm. **b**, Ubiquitin-positive inclusions in neurons. Sections of medulla from *Atg5*$^{flox/flox}$; nestin-*Cre* mice at six weeks of age were stained with an antibody against NeuN (a neuron-specific nuclear protein) and ubiquitin. Nuclei were stained with Hoechst 33258. Scale bar, 10 μm. **c**, Immunoelectron microscopy of ubiquitin-positive inclusion bodies. DRG neurons isolated from *Atg5*$^{-/-}$ neonates were analysed by immunoelectron microscopy using an anti-ubiquitin antibody. Scale bars, 500 nm.

demonstrated the specific association of ubiquitin with amorphous, occasionally filamentous, structures (Fig. 3c, left), as well as with more compact structures surrounded by filamentous materials (Fig. 3c, right; see Supplementary Fig. S5 for larger images). Outside the brain, *Atg5*$^{-/-}$ neonates showed inclusion body formation in the liver, the anterior lobe of pituitary gland (Supplementary Fig. S1) and the adrenal gland (data not shown).

Histological examination of *Atg5*$^{-/-}$ and *Atg5*$^{flox/flox}$; nestin-*Cre* mice suggested that, in addition to the presence of inclusion bodies, the intensity of diffuse cytoplasmic ubiquitin staining was higher compared with wild-type mice. We thus analysed the time course of accumulation of diffuse ubiquitinated proteins and inclusions in DRG neurons (the neonatal tissue in which inclusion body formation was most striking). DRG neurons from *Atg5*$^{-/-}$ embryos at E13.5 had no apparent abnormality. However, at E15.5, some neurons had accumulated diffuse, cytosolic ubiquitinated proteins with infrequent inclusions (Fig. 4a). Later, in newborn (postnatal day (P)0) *Atg5*$^{-/-}$ mice, multiple ubiquitin-positive inclusion bodies were present in DRG neurons. Thus, the accumulation of diffuse abnormal proteins seems to be the primary cellular phenotype of *Atg5*$^{flox/flox}$; nestin-*Cre* neurons. We obtained similar results using a biochemical method with whole brains. Polyubiquitinated proteins that accumulated in *Atg5*$^{flox/flox}$; nestin-*Cre* brains were primarily Triton-soluble in six-week-old mice (Fig. 4b). In contrast, in 14-week-old mice, Triton-insoluble polyubiquitinated proteins were also abundant, suggesting that inclusion body formation is a later event.

We confirmed these observations using hepatocytes, another cell type that showed extensive inclusion body accumulation under autophagy-defective conditions[11] (Supplementary Fig. S1). We crossed *Atg5*$^{flox/flox}$ mice with CAG-*Cre* mice that express Cre recombinase ubiquitously (see Methods)[20]. As recombination efficiency was not high when crossed with our *Atg5*$^{flox/flox}$ mice, the resulting mice (*Atg5*$^{flox/flox}$; CAG-*Cre*) were mosaic for the mutant allele and viable. In the livers of these mice, the *Atg5* gene was deleted in only about 30% of hepatocytes (Supplementary Fig. S6), which allowed us to compare directly the immunoreactivity of knockout cells with that of wild-type cells in the same specimen. Anti-ubiquitin staining of the liver in four-month-old *Atg5*$^{flox/flox}$; CAG-*Cre* mice showed that about 30% of cells had very high levels of diffuse cytoplasmic signals (in addition to inclusion bodies), compared with surrounding cells that were probably wild type (Fig. 4c). The results clearly demonstrate that cytosolic ubiquitinated proteins also accumulate in *Atg5*$^{-/-}$ hepatocytes.

We then determined the time course of accumulation of ubiquitinated proteins using Mx1-*Cre* transgenic mice[21]. In this system, Cre recombinase is expressed under the control of an interferon-responsive promoter that can be activated by application of polyinosinic acid-polycytidylic acid (pIpC), an interferon-inducible, synthetic double-stranded RNA. The *Atg5* gene in *Atg5*$^{flox/flox}$; Mx1-*Cre* liver was deleted by intraperitoneal injection of pIpC. Soon after injection, most targeted cells showed only diffuse ubiquitin staining, with no inclusion bodies (Fig. 4d, e). In contrast, large, ubiquitin-positive inclusion bodies were present in almost all targeted hepatocytes 16 days after pIpC injection (arrowheads in Fig. 4d). Cells with only inclusion bodies but not diffuse cytoplasmic staining were observed very rarely. Taken together, our data demonstrate that loss of autophagy first leads to accumulation of diffuse abnormal proteins, followed by generation of inclusion bodies.

We have shown that the inhibition of autophagy in neural cells causes neurodegeneration and symptoms of neurological pathology. As the mouse model we used does not express any disease-associated mutant proteins, the phenotype of these mutant mice indicates that autophagy mediates essential and continuous turnover of intracellular proteins. This system is particularly important for neurons, in which deregulation of this degradation process can induce cell dysfunction. The role of autophagy could be even more critical if

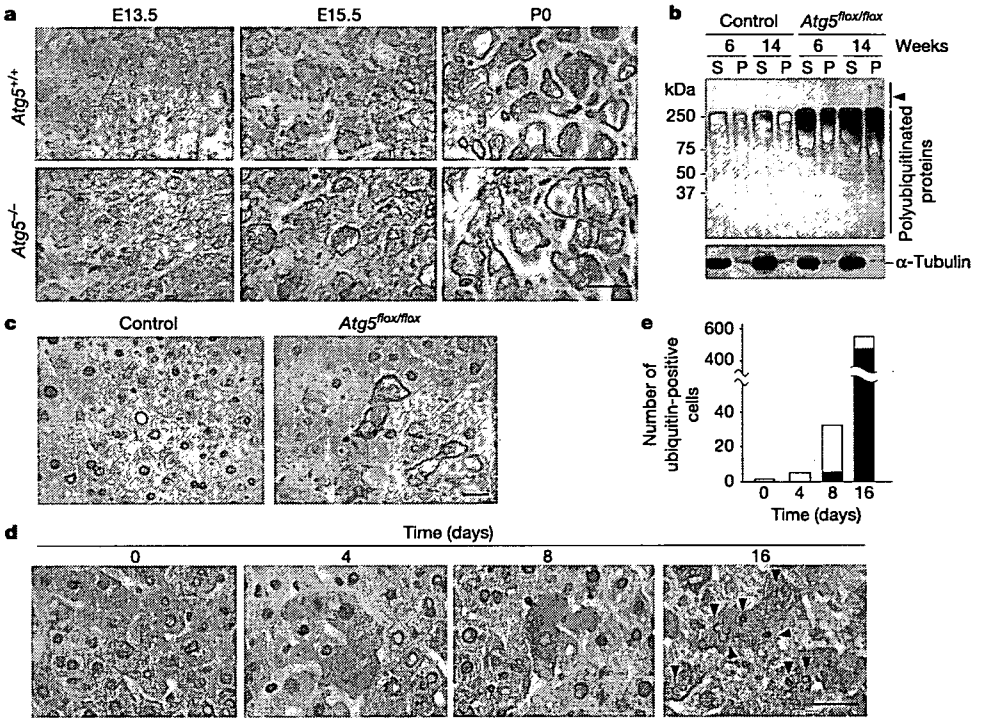

Figure 4 | Accumulation of diffuse ubiquitinated proteins in autophagy-defective cells. a, Immunohistochemistry of DRG neurons from $Atg5^{+/+}$ and $Atg5^{-/-}$ mice at different developmental stages (embryonic day (E)13.5, E15.5 or postnatal day (P)0), stained with an antibody directed against ubiquitin. Scale bar, 25 μm. **b,** Accumulation of Triton-X-100-soluble polyubiquitinated proteins in the brains of $Atg5^{flox/flox}$; nestin-*Cre* mice. Brain homogenate prepared at the indicated times from control ($Atg5^{flox/+}$; nestin-*Cre*) and $Atg5^{flox/flox}$; nestin-*Cre* ($Atg5^{flox/flox}$) mice were separated into Triton-X-100-soluble (S) and -insoluble (P) fractions and analysed by immunoblotting using anti-ubiquitin antibodies. Arrowhead indicates the stacking gel. **c,** Immunohistochemistry of liver sections from control ($Atg5^{flox/+}$; CAG-*Cre*) and $Atg5^{flox/flox}$; CAG-*Cre* ($Atg5^{flox/flox}$) mice at four months of age, using an anti-ubiquitin antibody. Scale bar, 25 μm. **d,** Immunohistochemistry of liver sections from six-week-old $Atg5^{flox/flox}$; Mx1-*Cre* mice at the indicated time points after pIpC injection, using anti-ubiquitin antibodies. Arrowheads indicate ubiquitin-positive inclusion bodies. Scale bar, 25 μm. **e,** Five thousand hepatocytes were randomly selected, and the number of cells with diffuse cytosolic ubiquitin signals, with (black) or without (white) inclusion bodies, were counted.

any aggregation-prone mutant proteins were expressed. Although autophagy is generally thought to be a non-selective process, several studies have suggested that autophagosomes can specifically engulf inclusion bodies[8,22]. In our system, however, inclusion bodies appeared in later phases of autophagy deficiency, suggesting that the primary role of autophagy under normal conditions is the turnover of diffuse cytosolic proteins, not direct elimination of inclusion bodies. As the population of ubiquitinated proteins in $Atg5^{flox/flox}$; nestin-*Cre* brains was similar to that in wild-type mouse brains, we suggest that cytoplasmic proteins that are usually ubiquitinated, rather than specific proteins, accumulate in larger amounts in the absence of autophagy (Supplementary Fig. S7). Downregulation of protein turnover could cause the accumulation of abnormal proteins, which then could promote aggregate formation (Supplementary Fig. S8).

The critical role of autophagy in the basal turnover of diffuse cytosolic proteins in neural cells should be emphasized, because it has been suggested that large inclusion bodies themselves might not be pathogenic, but that mutant proteins present diffusely in the cytosol could be the primary source of toxicity[23–27]. However, we do not rule out the possibility that autophagosomes can selectively recognize abnormal soluble proteins or microaggregates on the membrane surface. It was recently reported that the polyubiquitin-binding protein p62/SQSTM1 might mediate the specific recognition of protein aggregates by autophagosomes[28]. This pathway might also be involved in the degradation of diffuse ubiquitinated proteins by autophagy.

METHODS

Generation of tissue-specific *Atg5*-deficient mice. An approximately 1-kb *XbaI–SpeI* mouse genomic fragment containing putative exon 3 of the *Atg5* gene was flanked by two *loxP* sites containing the neomycin-resistant (*neo*^{r}) cassette from pMC1-Neo (Stratagene). The diphtheria toxin A (*DT-A*) gene was inserted downstream of the short arm, for negative selection against random integration of the vector (Supplementary Fig. S2). Targeted CCE embryonic stem cells of 129/SvEv mouse origin were injected into C57BL/6 blastocysts, and chimaeric mice were crossed with C57BL/6 mice to obtain $Atg5^{flox/+}$ mice. We used the following primers to detect wild-type *Atg5* and $Atg5^{flox}$ alleles: A (exon3-1), 5′-GAATATGAAGGCACACCCCTGAAATG-3′; B (short2), 5′-GTACTGCATAATGGTTTAACTCTTGC-3′; C (check2), 5′-ACAACGTCGAG CACAGCTGCGCAAGG-3′; D (5L2), 5′-CAGGGAATGGTGTCTCCCAC-3′; E (cre1), 5′-AGGTTCGTTCACTCATGGA-3′; F (cre2), 5′-TCGACCAGTTT AGTTACCC-3′.

Southern blot analysis was performed using the probe shown in Supplementary Fig. S2 after digestion of genomic DNA with *Eco*RV and *Kpn*I, as described previously[13]. Nestin-*Cre* transgenic mice expressing Cre recombinase under the control of the mouse nestin gene promoter and second intronic neural enhancer (a gift from S. Noguchi) have been described previously[29]. CAG-*Cre* transgenic mice expressing Cre recombinase under the control of the CAG (CMV enhancer and chicken β-actin) promoter have been described previously[20]. Mx1-*Cre* transgenic mice were obtained from the Jackson Laboratory[21]. Progeny containing the $Atg5^{flox}$ allele were bred with these *Cre* transgenic mice to generate $Atg5^{flox/flox}$; nestin-*Cre*, $Atg5^{flox/flox}$; CAG-*Cre* and $Atg5^{flox/flox}$; Mx1-*Cre* mice. $Atg5^{-/-}$ mice have been described previously[10]. All animal experiments were approved by the institutional committee of the Tokyo Metropolitan Institute of Medical Science.

Antibodies. A monoclonal antibody against ubiquitin (1B3) was purchased from

MBL and used for immunohistochemistry. Rabbit anti-ubiquitin polyclonal antibody (DakoCytomation) was used for immunoelectron microscopy. Anti-polyubiquitin monoclonal antibody (FK2, Nippon Bio-Test Laboratories) was used in immunoblot analyses. The following antibodies were also used: anti-NeuN monoclonal antibody (Chemicon), rabbit anti-calbindin polyclonal antibody (Chemicon), Alexa Fluor 488- and 660-conjugated goat anti-rabbit IgG (H + L) antibodies (Molecular Probes), monoclonal anti-glycogen synthase kinase-3β antibody (BD Biosciences), monoclonal anti-α-tubulin antibody (DM1A, Sigma-Aldrich), and antibodies against Atg5 (SO4)[13] and LC3[14].

Behavioural analysis. Mice were placed on a rod rotating at 20 r.p.m., and the time taken for them to fall from the rod was measured. If a mouse stayed on the rod until the end of the 2-min trial, a time of 120 s was recorded.

Immunohistochemical analysis. Mice were transcardially perfused with 4% paraformaldehyde in phosphate buffer (pH 7.4). Tissues were post-fixed in the same fixative overnight and embedded in paraffin. Sections were stained using Meyer's H&E. For immunohistochemical analysis, all tissue sections were subjected to antigen retrieval using the microwave method (in 0.01 M citrate buffer for 10 min). After blocking, sections were incubated with primary antibodies for 1 h, followed by 30 min incubation with fluorescently labelled or biotinylated secondary antibodies that were detected using Histomouse-plus kits (Zymed Laboratories) and the Liquid DAB substrate chromogen system (DakoCytomation). Apoptotic cells were detected by TUNEL assay using an *in situ* cell death detection kit (Roche Diagnostic).

Immunoelectron microscopy. For immunoelectron microscopy, the post-embedding immuno-gold method was used to label tissue sections embedded with LR white resin (London Resin Co.) as previously described[30].

Preparation of detergent-soluble and -insoluble fractions. Mouse brains were homogenized in five volumes of ice-cold 0.25 M sucrose buffer (50 mM Tris-HCl pH 7.4, 1 mM EDTA) with protease inhibitors. Homogenates were centrifuged at 500*g* for 10 min at 4 °C, and the resulting supernatants were lysed with an equal volume of cold sucrose buffer containing 1% Triton X-100. Lysates were subjected to centrifugation at 13,000*g* for 15 min at 4 °C to separate supernatants (fractions soluble in 0.5% Triton-X-100) and pellets. Pellets were resuspended in 1% SDS in PBS (Triton-X-100-insoluble fractions).

Received 6 February; accepted 20 March 2006.
Published online 19 April 2006.

1. Cuervo, A. M. Autophagy: in sickness and in health. *Trends Cell Biol.* 14, 70–77 (2004).
2. Levine, B. & Klionsky, D. J. Development by self-digestion: molecular mechanisms and biological functions of autophagy. *Dev. Cell* 6, 463–477 (2004).
3. Klionsky, D. J. The molecular machinery of autophagy: unanswered questions. *J. Cell Sci.* 118, 7–18 (2005).
4. Mizushima, N. The pleiotropic role of autophagy: from protein metabolism to bactericide. *Cell Death Differ.* 12, 1535–1541 (2005).
5. Ravikumar, B., Duden, R. & Rubinsztein, D. C. Aggregate-prone proteins with polyglutamine and polyalanine expansions are degraded by autophagy. *Hum. Mol. Genet.* 11, 1107–1117 (2002).
6. Fortun, J., Dunn, W. A. Jr, Joy, S., Li, J. & Notterpek, L. Emerging role for autophagy in the removal of aggresomes in Schwann cells. *J. Neurosci.* 23, 10672–10680 (2003).
7. Ravikumar, B. *et al.* Inhibition of mTOR induces autophagy and reduces toxicity of polyglutamine expansions in fly and mouse models of Huntington disease. *Nature Genet.* 36, 585–595 (2004).
8. Iwata, A. *et al.* Increased susceptibility of cytoplasmic over nuclear polyglutamine aggregates to autophagic degradation. *Proc. Natl Acad. Sci. USA* 102, 13135–13140 (2005).
9. Mizushima, N., Ohsumi, Y. & Yoshimori, T. Autophagosome formation in mammalian cells. *Cell Struct. Funct.* 27, 421–429 (2002).
10. Kuma, A. *et al.* The role of autophagy during the early neonatal starvation period. *Nature* 432, 1032–1036 (2004).
11. Komatsu, M. *et al.* Impairment of starvation-induced and constitutive autophagy in *Atg7*-deficient mice. *J. Cell Biol.* 169, 425–434 (2005).
12. Betz, U. A., Vosshenrich, C. A., Rajewsky, K. & Muller, W. Bypass of lethality with mosaic mice generated by Cre–*loxP*-mediated recombination. *Curr. Biol.* 6, 1307–1316 (1996).
13. Mizushima, N. *et al.* Dissection of autophagosome formation using Apg5-deficient mouse embryonic stem cells. *J. Cell Biol.* 152, 657–667 (2001).
14. Kabeya, Y. *et al.* LC3, a mammalian homologue of yeast Apg8p, is localized in autophagosome membranes after processing. *EMBO J.* 19, 5720–5728 (2000).
15. Cote, F., Collard, J. F. & Julien, J. P. Progressive neuronopathy in transgenic mice expressing the human neurofilament heavy gene: a mouse model of amyotrophic lateral sclerosis. *Cell* 73, 35–46 (1993).
16. Mangiarini, L. *et al.* Exon 1 of the *HD* gene with an expanded CAG repeat is sufficient to cause a progressive neurological phenotype in transgenic mice. *Cell* 87, 493–506 (1996).
17. Kikuchi, T., Mukoyama, M., Yamazaki, K. & Moriya, H. Axonal degeneration of ascending sensory neurons in gracile axonal dystrophy mutant mouse. *Acta Neuropathol. (Berl.)* 80, 145–151 (1990).
18. Sotelo, C. Axonal abnormalities in cerebellar Purkinje cells of the 'hyperspiny Purkinje cell' mutant mouse. *J. Neurocytol.* 19, 737–755 (1990).
19. Lossi, L., Mioletti, S. & Merighi, A. Synapse-independent and synapse-dependent apoptosis of cerebellar granule cells in postnatal rabbits occur at two subsequent but partly overlapping developmental stages. *Neuroscience* 112, 509–523 (2002).
20. Sakai, K. & Miyazaki, J. A transgenic mouse line that retains Cre recombinase activity in mature oocytes irrespective of the *cre* transgene transmission. *Biochem. Biophys. Res. Commun.* 237, 318–324 (1997).
21. Kuhn, R., Schwenk, F., Aguet, M. & Rajewsky, K. Inducible gene targeting in mice. *Science* 269, 1427–1429 (1995).
22. Kopito, R. R. Aggresomes, inclusion bodies and protein aggregation. *Trends Cell Biol.* 10, 524–530 (2000).
23. Saudou, F., Finkbeiner, S., Devys, D. & Greenberg, M. E. Huntingtin acts in the nucleus to induce apoptosis but death does not correlate with the formation of intranuclear inclusions. *Cell* 95, 55–66 (1998).
24. Kuemmerle, S. *et al.* Huntington aggregates may not predict neuronal death in Huntington's disease. *Ann. Neurol.* 46, 842–849 (1999).
25. Taylor, J. P. *et al.* Aggresomes protect cells by enhancing the degradation of toxic polyglutamine-containing protein. *Hum. Mol. Genet.* 12, 749–757 (2003).
26. Arrasate, M., Mitra, S., Schweitzer, E. S., Segal, M. R. & Finkbeiner, S. Inclusion body formation reduces levels of mutant huntingtin and the risk of neuronal death. *Nature* 431, 805–810 (2004).
27. Tanaka, M. *et al.* Aggresomes formed by α-synuclein and synphilin-1 are cytoprotective. *J. Biol. Chem.* 279, 4625–4631 (2004).
28. Bjorkoy, G. *et al.* p62/SQSTM1 forms protein aggregates degraded by autophagy and has a protective effect on huntingtin-induced cell death. *J. Cell Biol.* 171, 603–614 (2005).
29. Mori, H. *et al.* Socs3 deficiency in the brain elevates leptin sensitivity and confers resistance to diet-induced obesity. *Nature Med.* 10, 739–743 (2004).
30. Yamamoto, A. *et al.* Stacks of flattened smooth endoplasmic reticulum highly enriched in inositol 1,4,5-trisphosphate ($InsP_3$) receptor in mouse cerebellar Purkinje cells. *Cell Struct. Funct.* 16, 419–432 (1991).

Supplementary Information is linked to the online version of the paper at www.nature.com/nature. A summary figure is also included.

Acknowledgements We thank H. Neko, M. Miwa and Y. Kabeya for technical assistance. We also thank J. Miyazaki for the donation of CAG-*Cre* transgenic mice, T. Yoshimori for the anti-LC3 antibody, E. Yamada for histological examination, M. Yuzaki for the rotarod analysis, and A. Kuma for discussion. We thank Z. Yue for critical reading of the manuscript. This work was supported in part by Grants-in-Aid for Scientific Research from the Ministry of Education, Culture, Sports, Science and Technology of Japan. The authors thank the Yamada Science Foundation and the Cell Science Research Foundation for their financial support.

Author Contributions T.H. performed most of the experiments to characterize the neuron-specific knockout mice. M.M. analysed *Atg5*$^{-/-}$ mice. K.N., Y.N., R.S.-M. and M.Y. generated *Atg5*^{flox} chimaeric mice. A.Y. performed electron microscopy. K.M. and I.S. performed histological analysis. H.O. provided nestin-*Cre* mice and participated in manuscript preparation. N.M. conceived the experiments and generated the targeting vector. T.H. and N.M. wrote the paper.

Author Information Reprints and permissions information is available at npg.nature.com/reprintsandpermissions. The authors declare no competing financial interests. Correspondence and requests for materials should be addressed to to N.M. (nmizu@rinshoken.or.jp).

MOLECULAR AND CELLULAR BIOLOGY, Apr. 2006, p. 2924–2935 Vol. 26, No. 8
0270-7306/06/$08.00+0 doi:10.1128/MCB.26.8.2924–2935.2006

Novel Role for RbAp48 in Tissue-Specific, Estrogen Deficiency-Dependent Apoptosis in the Exocrine Glands

Naozumi Ishimaru,[1] Rieko Arakaki,[1] Fumie Omotehara,[1] Koichi Yamada,[2] Kenji Mishima,[2] Ichiro Saito,[2] and Yoshio Hayashi[1]*

Department of Oral Molecular Pathology, Institute of Health Biosciences, The University of Tokushima Graduate School, 3 Kuramotocho, Tokushima 770-8504,[1] and Department of Pathology, Tsurumi University School of Dentistry, Tsurumi,[2] Japan

Received 1 August 2005/Returned for modification 31 August 2005/Accepted 20 January 2006

Although tissue-specific apoptosis in the exocrine glands in estrogen-deficient mice may contribute to the development of autoimmune exocrinopathy, the molecular mechanism responsible for tissue-specific apoptosis remains obscure. Here we show that RbAp48 overexpression induces p53-mediated apoptosis in the exocrine glands caused by estrogen deficiency. RbAp48-inducible transfectant results in rapid apoptosis with p53 phosphorylation (Ser9) and α-fodrin cleavage. Reducing the expression of RbAp48 through small interfering RNA inhibits the apoptosis. Prominent RbAp48 expression with apoptosis was observed in the exocrine glands of C57BL/6 ovariectomized (OVX) mice but not in OVX estrogen receptor $\alpha^{-/-}$, $p53^{-/-}$, and $E2F\text{-}1^{-/-}$ mice. Indeed, transgenic expression of the RbAp48 gene induced apoptosis in the exocrine glands but not in other organs. These findings indicate that estrogen deficiency initiates p53-mediated apoptosis in the exocrine gland cells through RbAp48 overexpression and exerts a possible gender-based risk of autoimmune exocrinopathy in postmenopausal women.

Estrogenic action has been suggested to be responsible for the strong female preponderance of many autoimmune diseases, including systemic lupus erythematosus, rheumatoid arthritis, and Sjögren's syndrome (50, 51). Recent evidence suggests that apoptosis plays a key role in the physiology and pathogenesis of various autoimmune diseases (2, 7, 19, 35, 42). We have demonstrated that estrogenic action influences target epithelial cells through Fas-mediated apoptosis in a murine model for Sjögren's syndrome (13). Recently, we found that tissue-specific apoptosis in the exocrine glands spontaneously occurring in estrogen-deficient mice may contribute to the development of autoimmune exocrinopathy (14). We speculate that antiestrogenic actions might be a potent factor in the formation of pathogenic autoantigens. It has been reported that the antiestrogen tamoxifen (TAM) induces cell death in the human breast cancer cell line MCF-7 (17). We observed a time- and concentration-dependent increase in apoptosis of mouse and human salivary gland cells ([MSG] mouse primary culture; [HSG] human cell line) treated with TAM but not in other cell lines (HT-29, Colo201, and Jurkat) (14).

Apoptosis can be initiated by many different factors, but activation of caspases, which are a special class of proteolytic enzymes, is always involved in this process. Activation of caspases may be achieved by several molecular pathways; the best known stimuli triggering the caspase cascade are stimulation of Fas or TNF receptors, release of cytochrome *c* from the cellular mitochondria, and exposure to granzymes, which are secreted by cytotoxic T cells (3, 12, 31, 37, 54). Detailed research on the mechanisms controlling caspase activity will provide better insight into the pathogenesis of autoimmune diseases with special reference to estrogen deficiency. In this study, we have focused on the molecular mechanisms responsible for tissue-specific apoptosis caused by estrogen deficiency and identified RbAp48 as a novel apoptosis-inducing gene exclusively in the exocrine glands. Retinoblastoma (Rb) protein is a multifunctional protein that binds to transcription factors and kinases to regulate both cell growth and apoptosis (11). Although recent data suggest that loss of Rb can cause apoptosis through derepression of basally inhibited extrinsic apoptotic pathway genes (20), no mechanism has provided a molecular explanation for RbAp48 in the induction of apoptosis.

* Corresponding author. Mailing address: Department of Oral Molecular Pathology, Institute of Health Biosciences, The University of Tokushima Graduate School, 3 Kuramotocho, Tokushima 770-8504, Japan. Phone: 81 88 633 7327. Fax: 81 88 633 7327. E-mail: hayashi@dent.tokushima-u.ac.jp.

MATERIALS AND METHODS

Cell culture and gene transfection. HSG, MSG, HT29, Colo201, HeLa, HepG2, SH-SY5Y, NEC14, THP-1, Jurkat, Raji, U937, and W138 cells were cultured in Dulbecco's modified Eagle medium (DMEM) or RPMI 1640 medium containing 10% fetal bovine serum at 37°C. HSG and MSG cells have been described elsewhere (38, 40). The following were used for cell cultures: 10^{-7} M TAM (Wako Pure Chemical, Osaka, Japan), 10^{-9} M β-2-estradiaol (E2; Wako), 10^{-7} M staurosporin (Wako), paclitaxel (Wako), 1 μM etoposide (Wako), 1 μM ICI182780 (Wako), 25 ng/ml anti-Fas monoclonal antibody (MAb) (MBL, Nagoya, Japan), and 10 ng/ml recombinant human gamma interferon (R&D Systems, Minneapolis, MN). The RbAp48 gene inserted into the pCMV (2N3T) vector, a gift from D. Trouche, was transfected into the cells using FuGENE6 Transfection Reagent (Roche Diagnostics Corp., Indianapolis, IN). The RbAp48-stable cell line (RH0) from HSG cells in which RbAp48 expression was regulated by isopropyl-1-thio-β-D-galactopyranoside (IPTG), was established using a LacSwitch II Inducible Mammalian Expression System (Stratagene, La Jolla, CA). Briefly, the repressor vector (pCMVLacI) and RbAp48-inserted operator vector (pOPRVI/MCS) were cotransfected into HSG cells with FuGENE6, and the RbAp48 expression of hygromycin and G418-resistant transfectants was controlled by IPTG. For infection of adenovirus vector, RbAp48 gene-transfected MSG cells from $p53^{-/-}$ or wild-type mice were infected with 100 multiplicities of infection of adenovirus vector including the p53 gene obtained from Toren Finkel (National Institutes of Health). MSG and mouse mammary glands (MMG) were removed, placed in DMEM containing 10% fetal calf serum (FCS) and 10 mM HEPES (pH 7.4), and rapidly minced. The mate-

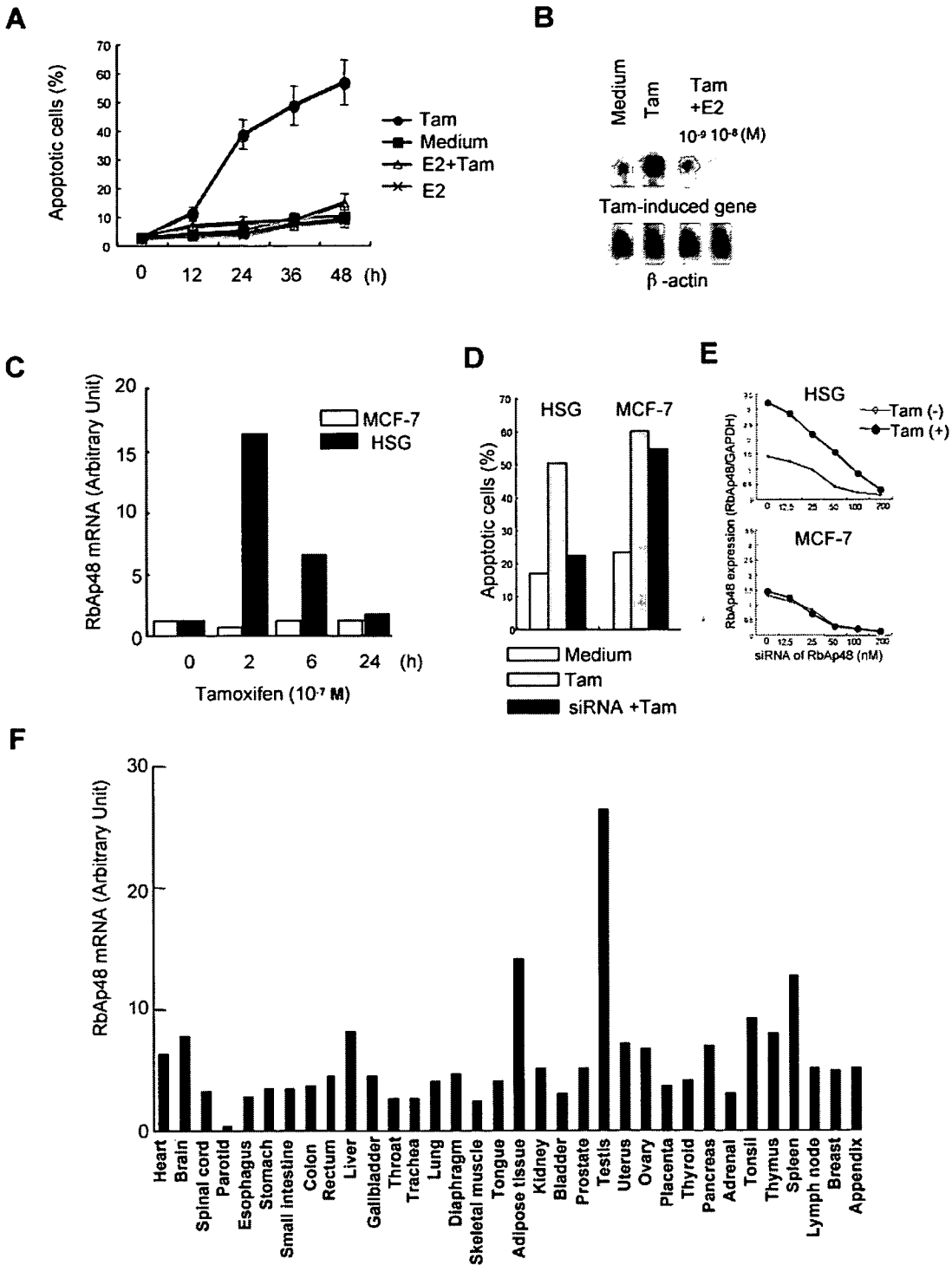

FIG. 1. Identification of the RbAp48 gene in salivary gland cell apoptosis. (A) A time-dependent increase in apoptotic HSG cells stimulated with TAM (10^{-7} M) was observed, and E2 (10^{-9} M) treatment inhibited apoptosis. Apoptotic cells were detected by flow cytometry using FITC-conjugated annexin V. (B) TAM-induced gene fragments cloned by differential display PCR were used as a probe by Northern blotting with mRNA from HSG cells treated with TAM (10^{-7} M) or E2 (10^{-9}M and 10^{-8}M). β-Actin mRNA was detected as an internal control. Each blot is representative of three independent experiments. (C) Analysis of RbAp48 mRNA expression was performed using total RNA from TAM-stimulated HSG and MCF-7 cells for 0 to 24 h. The graph is representative of three independent experiments. (D) The inhibitory effects of siRNA on TAM-induced apoptosis in HSG cells with siRNA (15 nM) of the RbAp48 construct but not in MCF-7 cells. After transfection of siRNA of RbAp48 and a fluorescence-labeled control gene, the cells were incubated with TAM (10^{-7} M) for an additional 24 h. Apoptosis was estimated by flow cytometric analysis using PE-conjugated annexin V. The graph is representative of three independent experiments. (E) A dose-dependent inhibition of siRNA (0 to 200 nM) of TAM-induced RbAp48 expression in HSG cells, not MCF-7 cells, was observed. The graph is representative of two independent experiments. (F) RbAp48 mRNA expression levels were analyzed using human tissue total RNA-blotted membrane. Message levels (arbitrary units) were quantified by BAS-2000II and expressed as the ratio of RbAp48 mRNA/β-actin mRNA. The graph is representative of two independent experiments.

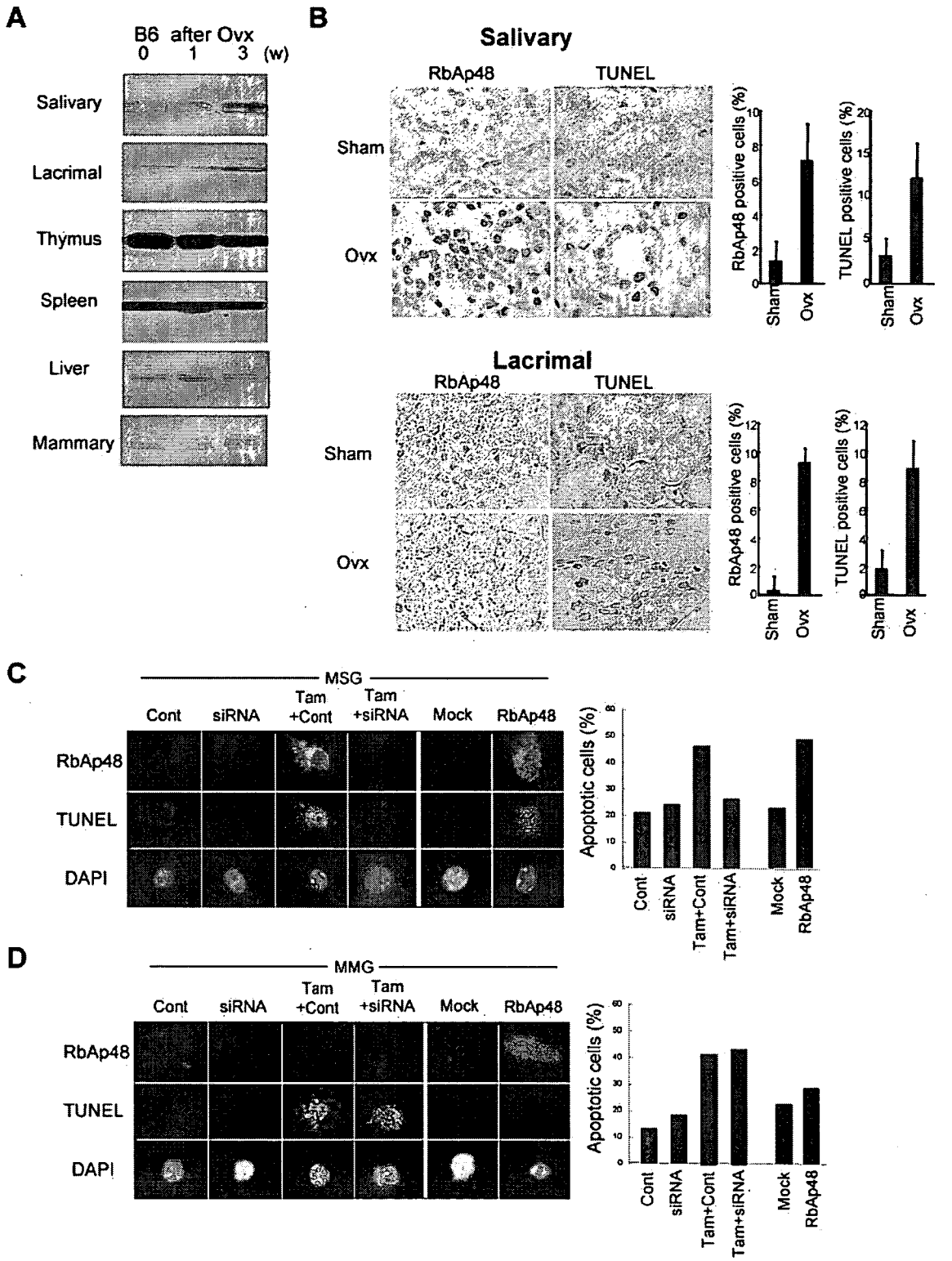

FIG. 2. RbAp48 overexpression in OVX B6 mice. (A) Increased RbAp48 expression in salivary and lacrimal gland tissues in OVX B6 mice from 0 to 3 weeks (age of mice, 4 to 7 weeks). Expression levels of RbAp48 in thymus, spleen, liver, and mammary glands from OVX B6 mice were constant. Western blot analysis was performed on proteins from tissue homogenates of OVX and sham mice. Blots were representative of three independent experiments. (B) Detection of $RbAp48^+$ and $TUNEL^+$ cells in salivary and lacrimal glands from OVX B6 and sham B6 mice at the age of 7 weeks. Immunohistochemical analysis of RbAp48 and in situ TUNEL assays were performed on the sections of salivary and lacrimal glands from OVX and sham mice. Images are representative of sections from five mice. The percentage of $RbAp48^+$ and $TUNEL^+$ cells in salivary and lacrimal glands was enumerated using a 10- by 20-mm grid covering an objective area of 0.16 mm^2. Data were analyzed in 10 fields per section and expressed as mean percent ± standard deviation of data from five mice. (C) TAM-induced apoptosis was associated with RbAp48 expression in

rials were then digested for 1 h at 37°C with 750 U/ml collagenase (Wako), 500 U/ml hyarulonidase type IV (Sigma), 1% bovine serum albumin, and 10 mM HEPES (pH 7.4) in DMEM. After digestion, they were filtered through a 70-μm nylon mesh, centrifuged, and rinsed twice with DMEM containing 10% FCS. These cells were cultured in chamber slides (Nalge Nunc International, Denmark) at a density of 5×10^4/well with DMEM containing 10% FCS. After cells were cultured for 24 h, the medium was changed to HuMedia-KG2 (Kurabo, Osaka, Japan).

Differential display analysis and Northern blotting. Total RNA was isolated from TAM-treated or nontreated HSG cells and reverse transcribed for differential display PCR with an RNAimage kit (Gene Hunter, Nashville, TN). TAM-induced cDNA fragments were gel excised and subcloned for TA vector. The clones were screened with a cDNA library derived from mRNA of TAM-stimulated HSG cells. The screened clone was transformed to plasmid and sequenced. Expressions of RbAp48 mRNA were detected by Northern blot analysis using ^{32}P-labeled RbAp48 cDNA probe. Equal loading of the gel was confirmed by using β-actin cDNA probe. In addition, the human total RNA-blotted membrane (Biocain Institute, Inc., San Leandro, CA) was used for analysis of RbAp48 mRNA in various human tissues.

Apoptosis detection assay. Apoptosis was detected using the annexin V-fluorescein isothiocyanate (FITC) apoptosis detection kit (Genzyme Corp., Cambridge, MA). Briefly, after cultured cells were washed with phosphate-buffered saline, the cells were incubated with FITC-conjugated annexin V and propidium iodide (PI) for 10 min at room temperature in the dark. Binding buffer was added, and apoptotic cells were detected by flow cytometric analysis with an EPICS flow cytometer (Beckman Coulter, Inc., Miami, FL).

Mice. Estrogen receptor α-deficient ($ER\alpha^{-/-}$), $p53^{-/-}$, $E2F\text{-}1^{-/-}$, or C57BL/6 (B6) mice were purchased from Taconic (Germantown, NY), Jackson Laboratory (Bar Harbor, ME), or Nihon Clea (Tokyo, Japan). These mice were subjected to ovariectomy (OVX mice) and or to a sham operation (sham mice) at 4 weeks of age. At 0 to 3 weeks after OVX, all organs were evaluated by pathological or immunohistochemical analysis. To generate the RbAp48-transgenic (TG) mice, B6 mice were used to obtain fertilized eggs, and the gene fragment containing RbAp48 cDNA regulated by salivary gland-specific promoter (22) (provided by B. B. Larsen) was microinjected into the pronucleus of fertilized eggs to establish the transgenic lines. Histopathological analysis of all organs of RbAp48-TG mice screened by PCR was performed. All mice were maintained in our specific-pathogen-free facility.

siRNA of RbAp48. Small interfering RNA (siRNA) corresponding to the coding sequence +136 to +156 of the RbAp48 gene was synthesized by Hokkaido System Science (Sapporo, Japan) according to standard methods (23, 52) for the following: sense, CGAGGAAUACAAAAUAUGGTT; antisense, CCA UAUUUUGUAUUCCUCGTT. siRNA of the glyceraldehyde-3-phosphate dehydrogenase (GAPDH) gene (Ambion, Austin, TX) was used as a control. siRNA (0 to 50 nM) and 1 μg of pCMV-green fluorescent protein (GFP) plasmid were cotransfected into HSG, MCF-7 cells, and the IPTG-controlled RbAp48-stable cell line (RH0) using a Silencer siRNA Transfection II Kit (Ambion) or FuGENE6 (Roche). At 24 h after cotransfection, RH0 cells were incubated with IPTG for an additional 24 h. GFP^+ apoptotic cells were detected by flow cytometry using phycoerythrin (PE)-conjugated annexin V.

E2F-1, ARF, and p53 siRNA. For siRNA of E2F-1, ARF, and p53, an siTrio Full Set (B-Brigde International, Sunnyvale, CA) was used for HSG cells. Briefly, each cocktail including the three RNA oligonucleotides listed below was transfected into cells with a Quick-Step Transfection Kit (B-Brigde International). Sequences of the oligonucleotide sets are as follows: for E2F-1, CCAACGUCCU UGAGGGCAUTT (sense), AUGCCCUCAAGGACGUUGGTT (antisense), CU GCAGAGCAGAUGGUUAUTT (sense), AUAACCAUCUGCUCUGCAGTT (antisense), GGAAAGUGAGGGAGGGAGATT (sense), and UCUCCCUCCC UCACUUUCCTT (antisense); for ARF, GCUCACCUCUGGUGCCAAATT (sense), UCACCAAGAACCUGCGCACTT (antisense), GGGUUUUCGCGGU UCACAUTT (sense), AUGUGAACCACGAAAACCCTT (antisense), GGGUU UUCGUGGUUCACAUTT (sense), and AUGUGAACCACCACGAAAAC CCTT (antisense), for p53, GGAAACUACUUCCUGAAAATT (sense), UUUU CAGGAAGUAGUUUCCTT (antisense), CUGGAAGACUCCAGUGGUATT (sense), UACCACUGGAGUCUUCCAGTT (antisense), CUUAGUACCUAAA AGGAAATT (sense), and UUUCCUUUUAGGUACUAAGTT (antisense). Transfected cells were incubated with or without TAM, and confocal or flow cytometric analysis was performed.

Western blotting. Whole-cell extracts of HSG or RH0 cells were purified using radioimmunoprecipitation assay buffer (50 mM Tris-HCl, pH 7.4, 150 mM NaCl, 1 mM EDTA, 1% NP-40, 1 mM dithiothreitol [DTT], 1 mM phenylmethylsulfonyl fluoride) supplemented with a protease inhibitor cocktail (Sigma Chemical Co., St. Louis, MO). After centrifugation for 20 min at 12,000 rpm at 4°C, the supernatant was extracted and used for samples. Also, to detect α-fodrin in organs, tissue samples from OVX and sham C57BL/6 mice were extracted as described above. Ten micrograms of each sample per well was used for 7.5 to 12.5% sodium dodecyl sulfate-polyacrylamide gel electrophoresis and transferred to polyvinylidene difluoride membranes, which were probed with anti-RbAp48, anti-Rb (p110 and p130), anti-Bad, anti-Bax, anti-ARF (p14 and p19), anti-cyclin D3 (BD Transduction Laboratories, Lexington, KY), anti-Mdm2, anti-E2F-1, anti-phospho-Rb (Sigma), anti-p53, anti-phospho-p53 Ab sampler kit (Ser6, Ser9, Ser15, Ser20, Ser37, Ser46, and Ser392; Cell Signaling Technology Inc., Beverly, MA), anti-α-fodrin (Affiniti, Mamhead, United Kingdom), and anti-p21 (Santa Cruz Biotechnology, Santa Cruz, CA) as the primary Abs, and anti-α-tubulin, GAPDH, or histone MAb (Sigma) as internal control. The nitrocellulose membranes were incubated with peroxidase-conjugated horse anti-mouse or rabbit immunoglobulin G (IgG; Vector Laboratories) as the secondary Ab. Protein binding was visualized with ECL Western blotting reagent (Amersham Corp., Arlington Heights, IL).

TUNEL assay. Apoptotic cells were detected in sections using the in situ terminal deoxynucleotidyltransferase (TdT)-mediated dUTP-biotin nick end labeling (TUNEL) kit (Wako). Sections were incubated with proteinase K (20 μg/ml) for 10 min and then presoaked in TdT buffer (0.5 μM cacodylate, 1 mM CoCl, 0.5 μM DTT, 0.05% bovine serum albumin, 0.15 M NaCl) for 10 min. Sections were incubated for 2 h at 37°C in 25 μl of TdT solution, containing 1× terminal transferase buffer, 0.5 nmol of biotin-dUTP, and 10 U of TdT. After the TdT reaction, sections were soaked in TdT blocking buffer (300 nM NaCl, 30 mM Tris-sodium citrate-2-hydrate), incubated with horseradish peroxidase-conjugated streptavidin for 30 min at room temperature, and developed for 10 min in phosphate-buffered citrate (pH 5.8) containing 0.6 mg/ml DAB (3,3'-diaminobenzidine-tetrahydrochloride-dihydrate). Nuclei were counterstained with hematoxylin. For confocal microscopic analysis, FITC-labeled UTP was used.

Caspase activity assay. Caspase activities were assayed using a caspase family colorimetric substrate set (BioVision Inc.). Briefly, 100 μg of cytoplasmic lysates of RH0 cells was incubated with 200 μM Ac-YVAD-pNA (caspase 1 substrate), Ac-VDVAD-pNA (caspase 2 substrate), Ac-DEVD-pNA (caspase 3 substrate), Ac-WEHD-pNA (caspase 5 substrate), Ac-VEID-pNA (caspase 6 substrate), Ac-IETD-pNA (caspase 8 substrate), and Ac-LEHD-pNA (caspase 9 substrate) at 37°C for 1 h. The absorbance of samples was read at 405 nm in a microtiter plate reader. The relative percent increase in caspase activity was determined by comparing these results with the level of the uninduced control.

Gel shift assay. Nuclear extracts were prepared from RH0 cells by a method previously described (29). Nuclear extracts containing 5 μg of protein were incubated in 20 μl of binding buffer (10 mM Tris-HCl, pH 8.0, 50 mM NaCl, 1 mM MgCl2, 0.5 mM DTT, and 4% glycerol) with or without a cold competitor. The E2F-1 DNA probe, 5'-TCCGTAGTTTTCGCGCTTAAATTTGAGAAAG GGCGCGAAACTAGTC-3' (10,000 cpm) labeled with [γ-^{32}P]ATP was added, and the samples were incubated at room temperature for 20 min. Reaction mixtures were separated in a 4% polyacrylamide gel and autoradiographed on X-ray film (Fujifilm, Kanagawa, Japan).

Immunohistochemical analysis. Immunohistochemical analysis of RbAp48 expression was performed on the sections of salivary and lacrimal glands from sham, OVX B6, RbAp48-WT (wild type), and RbAp48-TG mice. Paraffin-embedded sections were stained with anti-RbAp48 MAb (BD Transduction Laboratories) as the primary Ab. Protein binding was detected with an LSAB2 kit containing horseradish peroxidase (DAKO, Carpineteria, CA) and DAB as a substrate. The counterstaining of nuclei was performed with hematoxylin.

Confocal microscopy. Confocal microscopic analysis of RbAp48, E2F-1, ARF, and p53 expression, and TUNEL-positive cells was performed on the cultured cells, and frozen sections of salivary glands from sham, OVX $ER\alpha^{-/-}$, $p53^{-/-}$,

MSG cells from B6 mice, and the inhibitory effects with siRNA of RbAp48 construct were observed by confocal microscopic analysis. The percentage of $TUNEL^+$ apoptotic cells was enumerated as described. Cont, irrelevant siRNA control. Images are representative of three independent experiments. (D) TAM-induced apoptosis was not associated with RbAp48 expression in the primary culture of MMG cells from B6 mice. $TUNEL^+$ apoptotic cells were enumerated as described. Images are representative of three independent experiments.

$E2F1^{-/-}$, RbAp48-WT, and RbAp48-TG mice using a Confocal Laser Microscan (LSM 5 PASCAL; Carl Zeiss, Germany). As the second Abs, Alexa Fluor 488–anti-mouse IgG heavy and light chain [IgG (H+L)], Alexa Fluor 568–goat anti-rabbit IgG (H+L), Alexa Fluor 488–donkey anti-rat IgG (H+L), Alexa Fluor 488–chicken anti-goat IgG (H+L), and Alexa Fluor 568–rabbit anti-goat IgG (H+L) were used. Nuclear DNA was stained with 4′,6-diamidino-2-phenylindole dihydrochloride.

BrdU incorporation. MSG cells from RBAp48 TG and WT mice were stimulated with phorbol 12-myristate 13-acetate for 24 h, and 10 mM bromodeoxyuridine (BrdU) was incorporated for the last 2 h. Fixed and permeabilized cells were treated with DNase and stained with FITC-conjugated anti-BrdU antibody (BD Pharmingen, San Diego, CA). The polyvinylidene difluoride DNA synthetic activity was analyzed by flow cytometry.

RESULTS

Identification of TAM-induced gene. We found a time-dependent increase in apoptotic HSG cells stimulated with TAM, and E2 treatment inhibited the apoptosis (Fig. 1A). To identify gene products specific to TAM-induced apoptosis in the salivary gland cells, mRNAs from HSG cells treated with TAM and nontreated cells were analyzed by a differential display PCR method. From the samples isolated with the highest grade of differential expression, we analyzed the mRNAs from HSG cells treated with TAM and nontreated cells by a reverse Northern blotting technique (Fig. 1B). The sequence of TAM-induced mRNA corresponds (100%) to RbAp48. The expression of RbAp48 mRNA in HSG cells reached peak level at 2 h after stimulation with TAM, and then the level decreased, whereas increased expression of RbAp48 mRNA in MCF-7 cells was not observed (Fig. 1C). We confirmed the inhibitory effects of siRNA on TAM-induced apoptosis in HSG cells, not MCF-7 cells, with siRNA (5 to 50 nM) of RbAp48 construct (Fig. 1D). In addition, a dose-dependent inhibition of siRNA (0 to 200 nM) on TAM-induced RbAp48 expression in HSG cells, not MCF-7 cells, was observed (Fig. 1E). We next searched the tissue distribution of RbAp48 mRNA using human tissue total RNA-blotted membrane by Northern blot analysis. We found the highest level of expression of RbAp48 mRNA in the testis, which is consistent with the previous report (33), and the lowest was found in the parotid salivary gland (Fig. 1F), although the molecular mechanism by which the lowest RbAp48 mRNA is expressed in the parotid glands is unclear.

RbAp48 overexpression in estrogen-deficient mice. To confirm the in vivo overexpression of RbAp48 and apoptosis in estrogen-deficient B6 mice, OVX was performed on mice at the age of 4 weeks. Using Western blotting, we detected a time-dependent increase in RbAp48 in the salivary and lacrimal gland tissues from 0 to 3 weeks after OVX (at the age of 4 to 7 weeks) but not in other organs, including mammary glands (Fig. 2A). $RbAp48^+$ and $TUNEL^+$ apoptotic cells were detected by immunohistochemical analysis in the salivary and lacrimal gland sections from OVX B6 mice at the age of 7 weeks but not in sham mice (Fig. 2B). In vitro studies using primary cultured cells from B6 mice demonstrated that TAM-induced apoptosis was associated with RbAp48 expression in MSG cells but not in MMG cells (Fig. 2C and D). We confirmed the inhibitory effects of siRNA in MSG cells but not in MMG cells with siRNA of RbAp48 construct (Fig. 2C and D).

RbAp48 as a novel apoptosis-inducible gene. RbAp48 mRNA expression and apoptosis could be induced in HSG cells stimulated with TAM and a pure antiestrogen, ICI182780, but not with other apoptotic stimuli such as staurosporin, paclitaxel, anti-Fas MAb, and etoposide (Fig. 3A). This indicates that induction of RbAp48 mRNA expression might be dependent on estrogen deficiency. To ensure the role of RbAp48 in various types of cells, RbAp48 was transiently transfected, and apoptosis was determined by flow cytometry using an annexin V-FITC apoptosis detection kit. Among the cells examined (HSG, MSG, MCF-7, HT-29, Colo201, HeLa, HepG2, SH-SY5Y, NEC14, THP-1, Jurkat, Raji, U937, and WI38), significant apoptosis was induced exclusively in the salivary gland cells transfected with RbAp48 of both human and mouse origin (Fig. 3B). Notably, apoptosis was induced by transfection with RbAp48 cDNA in MSG cells isolated from $ER\alpha^{-/-}$ mice, indicating that this signaling might act in the downstream of estrogen-ER binding. Apoptotic cells could not be induced by the transgene of RbAp48 cDNA but was induced by TAM in MCF-7 cells. We confirmed that the induction levels of RbAp48 are the same in the other cell lines including Jurkat and THP-1 as the HSG cells (Fig. 3C). We next generated and analyzed the RbAp48-stable cell line (RH0), which was an IPTG-inducible transfectant of RbAp48 in HSG cells, with a LacSwitch II Inducible Mammalian Expression System using repressor and operator vectors. Apoptosis was drastically induced in IPTG-treated RH0 cells in association with RbAp48 expression within 8 h (Fig. 3D). When we examined the effect of siRNA on RbAp48-induced apoptosis, the apoptosis in IPTG-treated RH0 cells was clearly inhibited by siRNA of RbAp48 but not by siRNA of GAPDH or an irrelevant control (Fig. 3E).

Molecular mechanisms for RbAp48-induced apoptosis. We next examined the molecular mechanisms responsible for RbAp48-induced apoptosis. We detected upregulation of phosphorylated Rb, cyclin D3, p14ARF, Bax, Bad, cytochrome *c* (Cyt *c*) and a cleavage product of α-fodrin (arrow) in IPTG-treated RH0 cells (Fig. 4A). Our previous report demonstrated that α-fodrin is a candidate autoantigen of primary Sjögren's syndrome (10). When nuclear extracts of IPTG-treated RH0 cells were analyzed by gel shift assay, DNA binding activity of E2F-1 was detected in RbAp48-induced apoptotic cells (Fig. 4B). E2F-1 protein was also detected in the nuclear extract by Western blotting (Fig. 4B). It has been proposed that the E2F-1 transcription factor serves as a link between the Rb/E2F proliferation pathway and the p53 apoptosis pathway by inducing the expression of p14ARF, a protein that regulates p53 stability (36). We next focused on the p53-dependent pathway, because MSG cells transfected with RbAp48 isolated from $p53^{-/-}$ mice are apoptosis resistant (Fig. 4C). When Adp53-infected MSG cells were transfected with the RbAp48 gene, apoptosis was rapidly induced (Fig. 4C). Phosphorylated p53 (Ser9) was found by Western blotting after 2 to 4 h, but no other phosphorylated p53 (Ser15, Ser20, and Ser392) was detected (Fig. 4D). The phosphorylation of p53 in the other sites (Ser6, Ser37, and Ser46) was not observed (data not shown). We also confirmed a time-dependent downregulation of Mdm2 (Fig. 4D), which is important as a regulatory partner of p53 (47). Using Western blotting, we also detected increased p21 expression, a major player in the p53-mediated pathway, in IPTG-treated RH0 cells (Fig. 4E). p53 induces apoptosis by a multitude of molecular pathways, in addition to transactivation

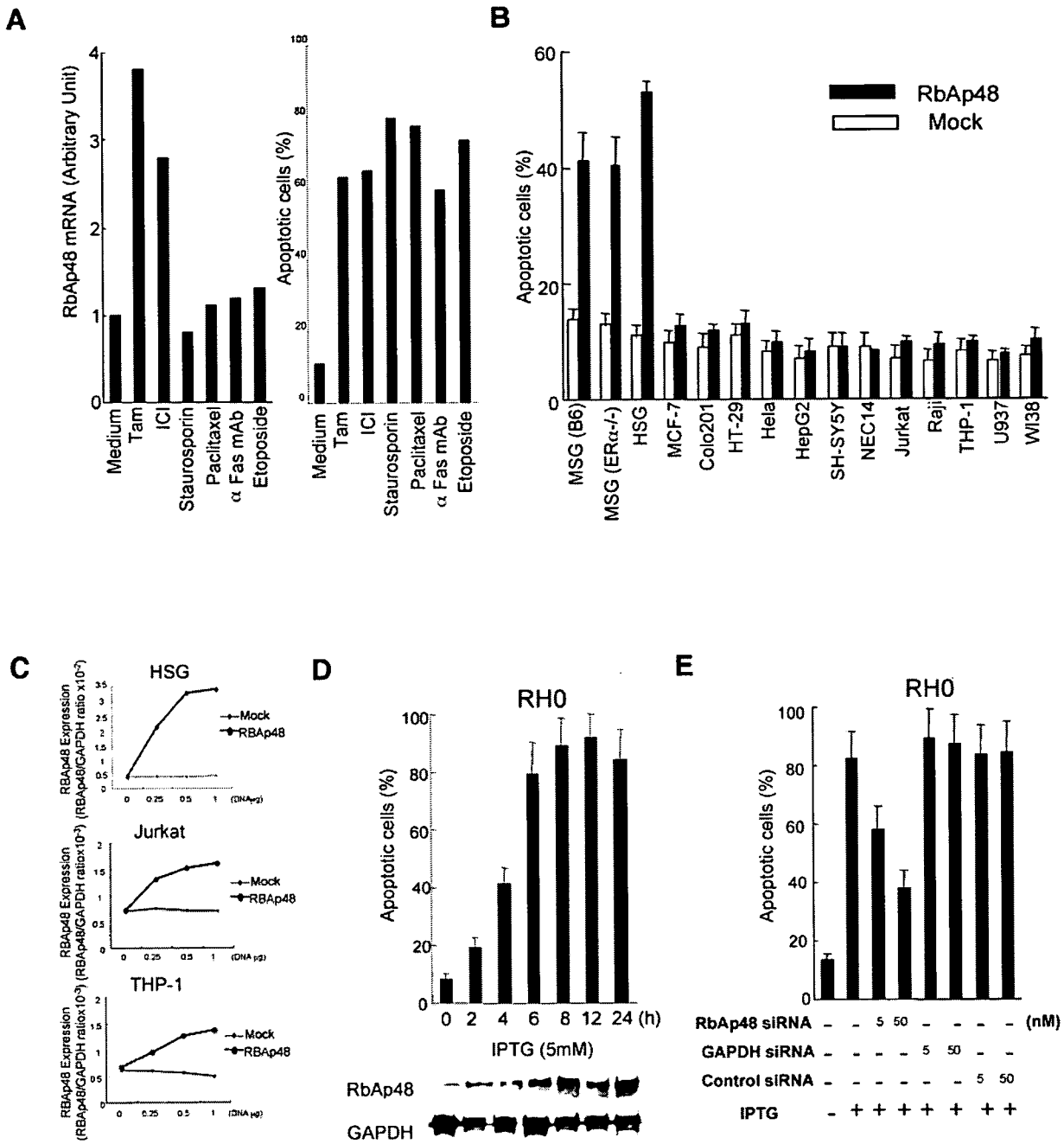

FIG. 3. Role of RbAp48 in salivary gland cell apoptosis. (A) HSG cells were treated with antiestrogenic reagents (10^{-7} M TAM and 10^{-7} M ICI182780) and general apoptotic stimuli (staurosporin, paclitaxel, anti-Fas MAb, and etoposide). RbAp48 mRNA was quantitated with BAS-2000II, and message level was expressed as the ratio of RbAp48 mRNA/β-actin mRNA; the percentage of apoptotic cells was detected by FITC-annexin V-PI was expressed for all of these agents. Graphs are representative of three independent experiments. (B) The RbAp48 gene was transiently transfected into various cells using FuGENE6. At 48 h after transfection of pCMV-RbAp48 plasmid or pCMV (mock) plasmid, apoptotic cells were detected by FITC-annexin V-PI. Data are the means ± standard deviations of triplicate samples. The graph is representative of three independent experiments. (C) The levels of the induction ratio of RbAp48 were shown to be the same in the other cell lines including Jurkat and THP-1 as the HSG cells using Western blot analysis. The levels were expressed as the ratio of RbAp48/GAPDH protein. (D) Establishment of the RbAp48 stable cell clone. An increase in RbAp48 expression and apoptosis of IPTG-treated RH0 cells were observed in a time-dependent manner. Apoptotic cells were detected by FITC-annexin V-PI. Data are means ± standard deviations of triplicate samples. Expressions of RbAp48 and GAPDH as an internal control were detected by Western blot analysis. Graph and images are representative of four independent experiments. (E) Inhibitory effects of siRNA on RbAp48-induced apoptosis. IPTG-treated RH0 cells were cotransfected with siRNA (5 to 50 nM) of RbAp48 and pCMV-GFP. Apoptotic cells gated on GFP^+ were detected by PE-conjugated annexin V. Data are means ± standard deviations of triplicate samples. Graph is representative of three independent experiments.

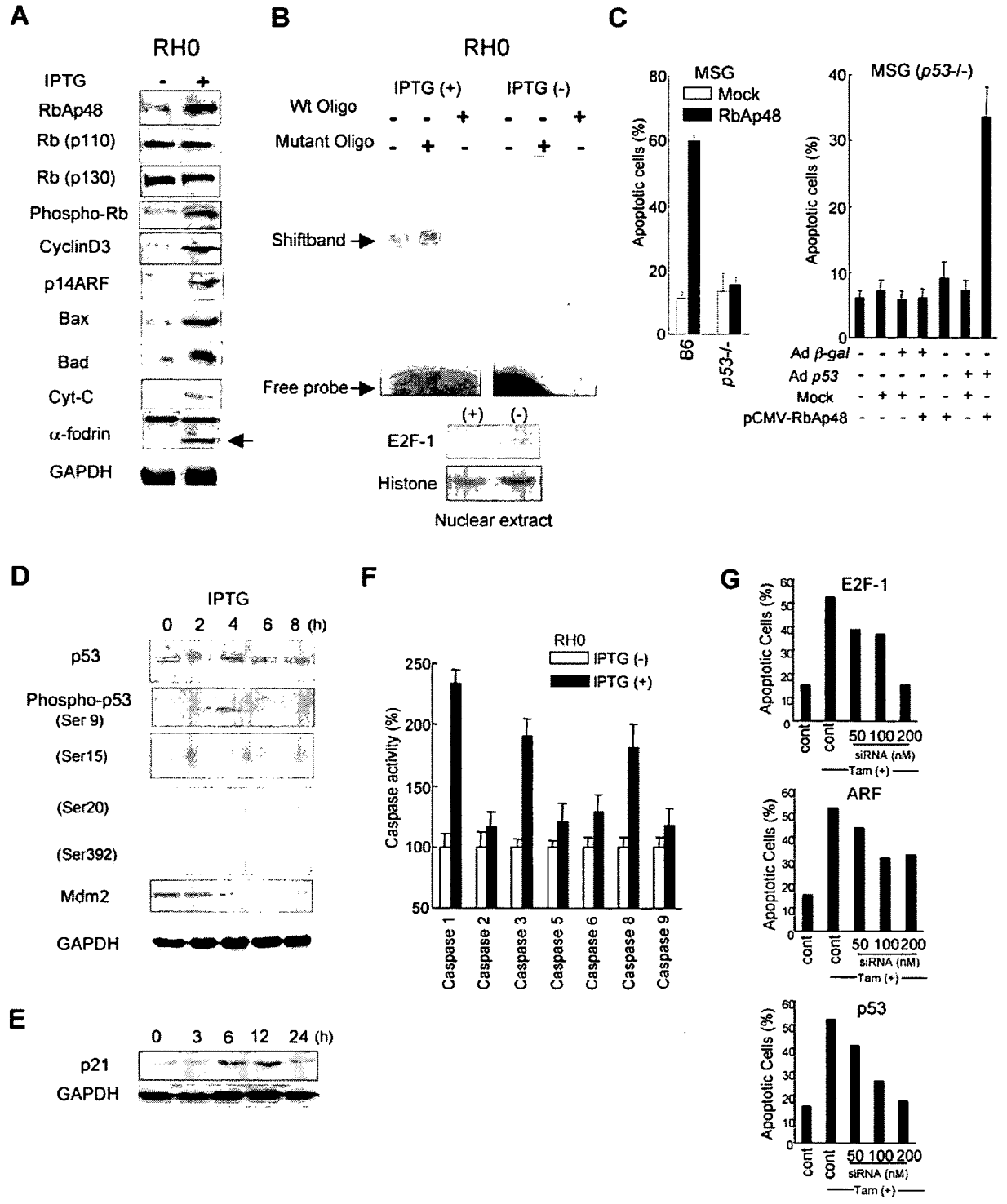

FIG. 4. Molecular mechanisms responsible for RbAp48-induced apoptosis. (A) Contribution of cell cycle and mitochondrion-related molecules in RbAp48-induced apoptosis of RH0 cells. The lysates of IPTG-treated or nontreated RH0 cells were used to detect RbAp48, Rb (p110 and p130), phospho-Rb, cyclin D3, p14ARF, Bax, Bad, Cyt-*c*, the cleavage product of α-fodrin, and GAPDH for Western blot analysis. Blots are representative of three independent experiments. (B) Detection of E2F-1 transcriptional activity in RbAp48-induced apoptosis. The nuclear proteins of IPTG-treated RH0 cells were analyzed by gel shift assay with an E2F-1 binding DNA probe. To confirm the specific binding to the E2F-1 binding site, the mutant oligonucleotide and wild-type oligonucleotide as a competitor were used for this assay. E2F-1 protein was detected in the nuclear extract by Western blotting. Histone was used for an internal control. Blots are representative of three independent experiments. (C) Apoptosis of MSG cells from $p53^{-/-}$ mice was not observed by RbAp48 gene transfection. Transfection with pCMV (Mock) was used as control. MSG ($p53^{-/-}$) cells were infected with Ad*p53* and incubated for 24 h. The infected cells were cotransfected with the RbAp48 gene and